GLIA

WILEY

RESEARCH ARTICLE

Developmental maturation and regional heterogeneity but no sexual dimorphism of the murine CNS myelin proteome

Sophie B. Siems[1] | Vasiliki-Ilya Gargareta[1] | Leonie C. Schadt[1] | Vinicius Daguano Gastaldi[2] | Ramona B. Jung[1] | Lars Piepkorn[3,4] | Patrizia Casaccia[5] | Ting Sun[1] | Olaf Jahn[3,4] | Hauke B. Werner[1,6]

[1]Department of Neurogenetics, Max Planck Institute for Multidisciplinary Sciences, Göttingen, Germany

[2]Clinical Neuroscience, Max Planck Institute for Multidisciplinary Sciences, Göttingen, Germany

[3]Neuroproteomics Group, Department of Molecular Neurobiology, Max Planck Institute for Multidisciplinary Sciences, Göttingen, Germany

[4]Translational Neuroproteomics Group, Department of Psychiatry and Psychotherapy, University Medical Center Göttingen, Göttingen, Germany

[5]Neuroscience Initiative, Advanced Science Research Center, The City University of New York, New York, New York, USA

[6]Faculty for Biology and Psychology, University of Göttingen, Göttingen, Germany

Correspondence
Olaf Jahn, Neuroproteomics Group, Department of Molecular Neurobiology, Max Planck Institute for Multidisciplinary Sciences, Göttingen, Germany.
Email: jahn@mpinat.mpg.de

Hauke B. Werner, Department of Neurogenetics, Max Planck Institute for Multidisciplinary Sciences, Göttingen, Germany.
Email: hauke@mpinat.mpg.de

Funding information
Deutsche Forschungsgemeinschaft, Grant/Award Number: WE 2720/4-1

Abstract

The molecules that constitute myelin are critical for the integrity of axon/myelin-units and thus speed and precision of impulse propagation. In the CNS, the protein composition of oligodendrocyte-derived myelin has evolutionarily diverged and differs from that in the PNS. Here, we hypothesized that the CNS myelin proteome also displays variations within the same species. We thus used quantitative mass spectrometry to compare myelin purified from mouse brains at three developmental timepoints, from brains of male and female mice, and from four CNS regions. We find that most structural myelin proteins are of approximately similar abundance across all tested conditions. However, the abundance of multiple other proteins differs markedly over time, implying that the myelin proteome matures between P18 and P75 and then remains relatively constant until at least 6 months of age. Myelin maturation involves a decrease of cytoskeleton-associated proteins involved in sheath growth and wrapping, along with an increase of all subunits of the septin filament that stabilizes mature myelin, and of multiple other proteins which potentially exert protective functions. Among the latter, quinoid dihydropteridine reductase (QDPR) emerges as a highly specific marker for mature oligodendrocytes and myelin. Conversely, female and male mice display essentially similar myelin proteomes. Across the four CNS regions analyzed, we note that spinal cord myelin exhibits a comparatively high abundance of HCN2-channels, required for particularly long sheaths. These findings show that CNS myelination involves developmental maturation of myelin protein composition, and regional differences, but absence of evidence for sexual dimorphism.

KEYWORDS
axon/glia-interaction, myelin maturation, oligodendrocyte, quantitative proteomics, white matter

1 | INTRODUCTION

Oligodendrocytes support neuronal functions throughout the CNS. Their cellular processes expand into myelin sheaths that enwrap and insulate axonal segments, thereby enabling both rapid and precise propagation of action potentials (Hartline & Colman, 2007; Tasaki, 1939). They also support axonal homeostasis by providing specialized extracellular vesicles (Chamberlain et al., 2021; Frühbeis et al., 2020) and energy substrates for axonal mitochondria (Fünfschilling et al., 2012; Lee et al., 2012; Looser et al., 2024; Späte et al., 2024), counteracting reactive oxygen species (Kassmann et al., 2007; Mukherjee et al., 2020), and maintaining ion homeostasis upon axonal activity (Kapell et al., 2023; Marshall-Phelps et al., 2020). Indeed, oligodendroglial functions are required to prevent the degeneration of myelinated axons. Structurally, axons and their myelin sheaths are linked by adhesion proteins (Djannatian et al., 2019; Elazar, Vainshtein, Golan, et al., 2019; Elazar, Vainshtein, Rechav, et al., 2019; Nguyen et al., 2009). Together, myelin proteins are critical for biogenesis and maintenance of the axon/myelin-unit and the functions of oligodendrocytes in axonal support.

Systematic investigations of the molecular composition of myelin membranes have benefitted from their comparatively high lipid content and thus low hydrated density, which allowed the development of protocols for the biochemical isolation of highly pure myelin-enriched fractions from nervous tissue via sucrose density gradient ultracentrifugation and osmotic shocks (Autilio et al., 1964; Erwig, Hesse, et al., 2019; Haley et al., 1981; Korey et al., 1958; Norton & Poduslo, 1973). Early systematic assessment of CNS myelin proteins involved separating myelin fractions by 1-dimensional SDS-PAGE and protein labeling by Fast Green (Morell et al., 1972) or Coomassie Blue (Magno-Sumbilla & Campagnoni, 1977). These approaches have visualized 3–5 bands, which are mainly constituted by exceptionally abundant myelin proteins that are now termed proteolipid protein (PLP), myelin basic protein (MBP), and cyclic nucleotide phosphodiesterase (CNP). More recently, myelin fractions have been assessed using "omics"-techniques, including lipidomics (Gopalakrishnan et al., 2013; Louie et al., 2023), transcriptomics (Thakurela et al., 2016), and proteomics (Manrique-Hoyos et al., 2012; Taylor et al., 2004; Vanrobaeys et al., 2005; Werner et al., 2007).

Since then, gel-free, label-free quantitative mass spectrometry (Distler et al., 2016) has emerged as very powerful in the systematic identification and simultaneous quantification of hundreds of distinct proteins in myelin fractions, thereby allowing comprehensive profiling of the CNS myelin proteome in mouse brains (Jahn et al., 2020). This reflects that the dynamic range of mass spectrometry is markedly higher compared to that of staining proteins in gels. Notwithstanding that only about 50 among these proteins have so far been visualized in myelin using independent, antibody-based techniques, and thus confirmed as "known myelin proteins," quantitative mass spectrometry has enabled the unbiased scrutiny of pathological myelin proteome profiles in several mouse models (Buscham et al., 2022; Erwig, Patzig, et al., 2019; Joseph et al., 2019; Patzig et al., 2016), and evolutionary comparisons of CNS myelin between zebrafish and mice (Siems et al., 2021). A recent analysis of myelin purified from the subcortical

white matter of humans (Gargareta et al., 2022) found that the abundance of the major structural myelin proteins, including PLP, MBP, and CNP, correlates well between humans and mice. However, multiple other distinct myelin proteins were identified predominantly or exclusively in human or mouse myelin, indicating species-dependent divergence of CNS myelin protein composition across mammalian species.

However, it is not known to which extent the CNS myelin proteome varies within the same species. Here, we use quantitative mass spectrometry to assess the proteome of myelin purified from mouse brains at postnatal day 18 (P18), P75, and 6 months. We find that the relative abundance of most structural myelin proteins, including MBP and CNP, remains largely similar over time. However, the abundance of the cytoskeleton-associated gelsolin (GSN), cofilin (CFL1, CFL2), and sirtuin-2 (SIRT2) decreases with myelin maturation. In contrast, the abundance of multiple other myelin proteins markedly increases with maturation, including the subunits of myelin septin filaments (SEPTIN2, SEPTIN4, SEPTIN7, and SEPTIN8), carbonic anhydrases (CA2, CA14), heat shock protein crystallin-αB (CRYAB), the antioxidative glutathione S-transferase-pi1 (GSTP1), and quinoid dihydropteridine reductase (QDPR). QDPR emerges as a highly specific antigenic marker for mature oligodendrocytes and myelin, thus complementing traditional oligodendroglial markers. Maturation of the myelin proteome is largely accomplished by P75. Importantly, no sex-dependent differences were detected, as male and female mice displayed essentially similar myelin proteomes at P75. Finally, comparing the proteomes of myelin-enriched fractions from corpora callosa, optic nerves, spinal cords, and cortices of male mice at P75 revealed that hyperpolarization-activated cyclic nucleotide-gated potassium and sodium channel 2 (HCN2), which enables the formation of particularly long sheaths (Swire et al., 2021), is comparatively abundant in spinal cord myelin. Together, our findings reveal that the developmental biogenesis of CNS myelin involves a step of maturation of its proteome. Sexual dimorphism of myelin protein composition was not evident.

2 | RESULTS

2.1 | Purification of myelin from CNS tissue and proteome analysis

We used an established protocol of sucrose density gradient centrifugation (Erwig, Hesse, et al., 2019) to biochemically enrich myelin as a light-weight membrane fraction from the brains of male mice at postnatal day 18 (P18), P75, and 6 months (Figure 1a), the brains of male and female mice at P75 (Figure 1b), and four CNS regions of male mice at P75 (Figure 1c). Myelin membranes accumulate at the interface between 0.32 and 0.85 M sucrose (Norton & Poduslo, 1973). When separating the purified myelin fractions by SDS-PAGE and staining the comprised proteins by silver staining, we observed a high reproducibility of myelin purification, but no signs of protein degradation (Supplemental Figure S1). The fractions were thus considered suitable for systematic analysis of their protein composition.
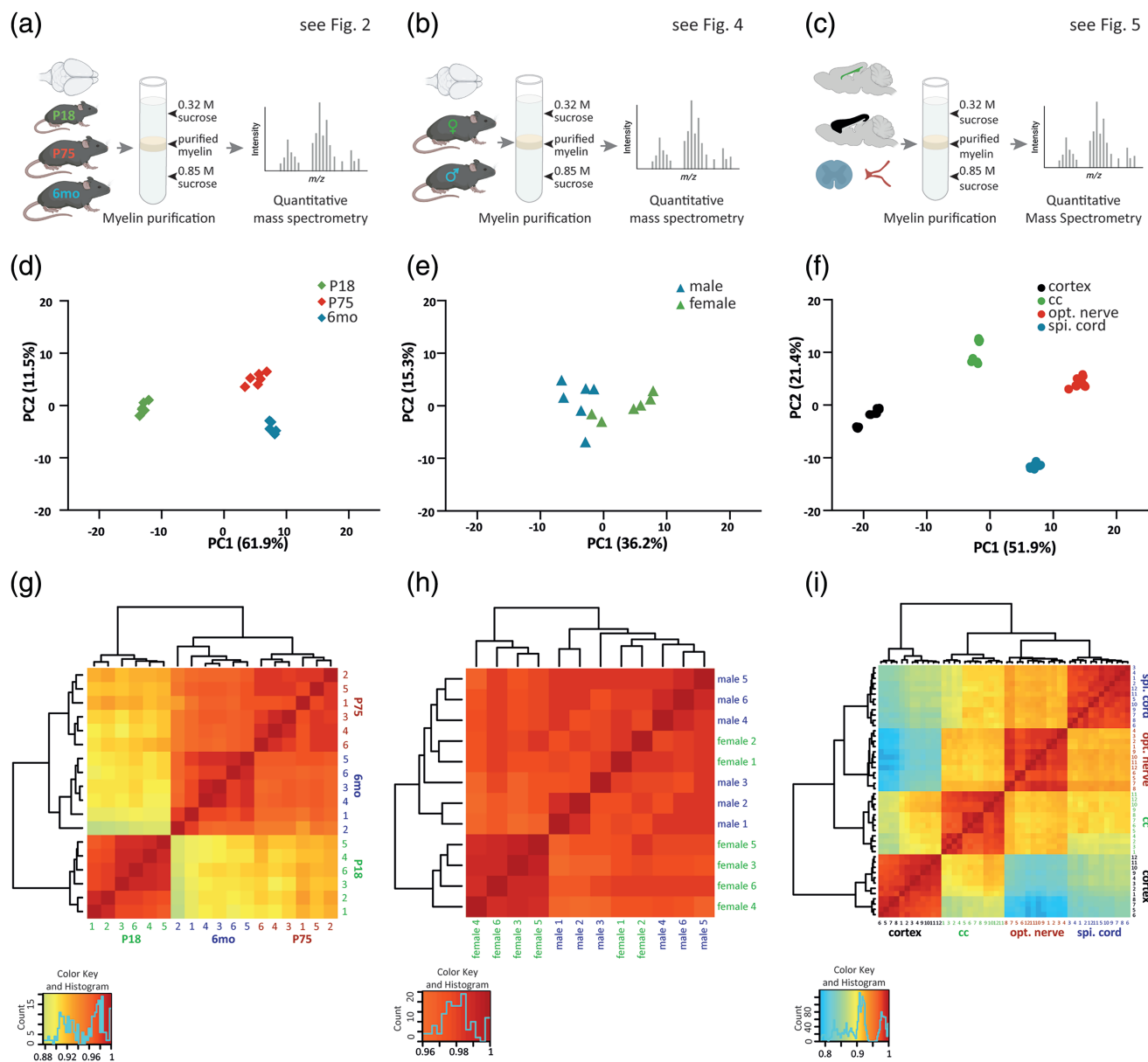
FIGURE 1 Proteome analysis to address myelin heterogeneity in mice. (a–c) Schematic of the workflow. Myelin was biochemically purified from the brains of male mice at three ages (P18, P75, 6 months) (a), brains of female and male mice at P75 (b), or four CNS regions of male mice at P75 (cortex, corpus callosum [cc], optic nerve [opt. nerve], and spinal cord [spi. cord]) (c). The protein composition of the myelin fractions was analyzed by quantitative mass spectrometry with $n = 3$ biological replicates per condition each, and two technical replicates at the tryptic digest level for the maturation- (a) and sex-dependent sample sets (b), or four technical replicates at both the digestion and injection level for the CNS regions sample set (c). For SDS-PAGE-separation of myelin fractions and silver staining of proteins see Supplemental Figure S1; for entire datasets see Supplemental Tables S1–S3. (d–f) Principal Component Analysis (PCA) of the UDMS^E proteome datasets of CNS myelin purified from the brains of male mice at P18, P75, and 6 months (d), the brains of male and female mice at P75 (e), and four CNS regions of male mice at P75 (f). Note that the PCA of the myelin proteome of both the three ages, and the four CNS regions, but not of the two sexes, shows evident clustering into distinct groups. (g–i) Clustered heatmaps showing Pearson's correlation coefficients for protein abundance, comparing the UDMS^E proteome datasets of CNS myelin purified from the brains of male mice at P18, P75, and 6 months (g), the brains of male and female mice at P75 (h), and four CNS regions of male mice at P75 (i). Note that myelin at P18 clusters away from myelin at P75 and 6 months (g), and that the CNS regions display evident clustering (i). Conversely, the proteomes of male and female myelin do not show evident clustering (h).

To this aim we solubilized the myelin fractions using high urea concentration and the zwitterionic detergent amidosulfobetain-14 (ASB-14), and subsequently subjected them to filter-aided sample preparation (FASP) for automated in-solution tryptic digest, ultra-performance liquid chromatography (nanoUPLC) for peptide fraction-ation, and data-independent acquisition (DIA) of data by electrospray

ionization quadrupole time-of-flight (ESI-QTOF) mass spectrometry (MS). We utilized two DIA-MS modes (MS^E, UDMS^E; for explanation see below), which both enable the simultaneous identification and quantification of all peptides entering the mass spectrometer. The correlation of peptide signal intensities with the known concentration of a spike-in protein digest (yeast enolase 1) thus allows the quantification of proteins (TOP3 method; Silva et al., 2006).

We then assessed the resulting datasets (Supplemental Tables S1–S3) by principal component analysis (PCA) (Figure 1d–f) and Pearson's correlation coefficients for protein abundance (Figure 1g–i). By both methods, the myelin proteome dataset at P18 clustered markedly away from those at P75 and at 6 months (Figure 1d,g). The myelin proteome at P75 and at 6 months also clustered away from each other, although less pronounced (Figure 1d,g). This implies that the protein composition of CNS myelin changes considerably during its maturation up to P75, and after that remains more similar up to an age of at least 6 months. When using PCA and Pearson's correlation coefficients to compare the myelin proteome of male and female mice, the datasets did not segregate into distinct clusters (Figure 1e,h). This indicates that myelin protein composition in the brains of female and male mice is essentially similar, at least at P75. When comparing the proteome of myelin purified from four CNS regions (Figure 1f,i), all datasets decidedly clustered away from each other. Yet, the proteome dataset of myelin purified from a gray matter region (the cortex) clustered further away from that of a white matter region (corpus callosum) or those of mixed regions (optic nerve, spinal cord). Together these data imply that the proteome of myelin depends on its maturation and the analyzed CNS region, but not on the sex of mice.

2.2 | Maturation of the myelin proteome

To visualize the changes of the myelin proteome coinciding with maturation, we displayed the datasets in volcano plots (Figure 2a,b). In agreement with the PCA and Pearson's correlation coefficients (Figure 1d,g), the volcano plot displayed considerable differences between the myelin proteome at P18 and P75 (Figure 2a), but only little variation between P75 and 6 months (Figure 2b).

To highlight the relative abundance of known myelin proteins we used heatmaps (Figure 2c). The mass spectrometry mode MS^E enables the quantification of myelin proteins with a dynamic range of over four orders of magnitude parts per million (PPM). MS^E is thus suited for reliable quantification of all identified myelin proteins (Gargareta et al., 2022; Jahn et al., 2020), but of particular relevance for quantification of the exceptionally abundant proteolipid protein (PLP), myelin basic protein (MBP), cyclic nucleotide phosphodiesterase (CNP), claudin 11 (CLDN11), myelin-associated glycoprotein (MAG), and myelin oligodendrocyte glycoprotein (MOG). On the other hand, the ultradefinition MS^E mode (UDMS^E), comprising an additional level of peptide separation by ion mobility spectrometry, identifies more than two times as many proteins in myelin compared to MS^E. However, UDMS^E displays a compressed dynamic range of only about three orders of magnitude PPM (Gargareta et al., 2022; Jahn et al., 2020). In the

following heatmaps comparing protein abundances, we will thus display PLP, MBP, CNP, CLDN11, MAG, and MOG according to data gained by MS^E, and all other myelin proteins according to UDMS^E.

We found that most structural myelin proteins displayed a similar relative abundance in myelin at all three ages, as exemplified by MBP, CNP, MAG, MOG, plasmolipin (PLLP), and tetraspanin-2 (TSPAN2) (Figure 2c). However, the abundance of several other myelin proteins in myelin increased with maturation, including that of PLP, N-myc downstream regulated-1 gene (NDRG1), contactin-2 (CNTN2), and peptidyl arginine deiminase 2 (PADI2) (Figure 2c). The abundance of all subunits of the myelin septin filament (SEPTIN2, SEPTIN4, SEPTIN7, and SEPTIN8) also increased with maturation, in agreement with a previous report (Patzig et al., 2016), as did that of the septin-associated cytoskeletal adaptor anillin (ANLN) (Figure 2c). Notably, several proteins that display a markedly increased abundance coinciding with myelin maturation may exert protective functions, including the carbonic anhydrases CA2 and CA14, the immunomodulatory tetraspanin CD82, the antioxidative glutathione S-transferase-pi1 (GSTP1), the small heat shock protein crystallin-αB (CRYAB), and quinoid dihydropteridine reductase (QDPR) (Figure 2c). On the other hand, multiple cytoskeleton-associated myelin proteins were more abundant in myelin at P18, that is, the actin-associated gelsolin (GSN) and cofilins (CFL1, CFL2), as well as the microtubule-associated sirtuin-2 (SIRT2) (Figure 2c). Importantly, these mass spectrometric comparisons were generally in agreement with immunoblot-based validation of selected of these proteins (Figure 2d). Together, these results imply that the protein composition of CNS myelin in the brains of mice matures between P18 and P75.

To approach if maturation-dependent changes of protein abundance in myelin (Figure 2) correlate with changes of transcript abundance in oligodendrocytes, we utilized previously published scRNA-seq datasets (GSE75330; Marques et al., 2016). These data allow the comparison of mRNA abundance in mature oligodendrocytes (MOL) of juvenile mice at age P18–P31 with those of adult mice at age P50–P90. To this aim, we evaluated the abundance of selected transcripts in all 1894 cells designated as mature oligodendrocytes (MOL) in juvenile and all 450 cells designated as MOL in mature mice (Supplemental Figure S2). Notably, however, only a subset of myelin-related genes displayed a similar trend in the mRNA abundance in MOL and protein abundance in myelin. For example, structural myelin proteins *Mbp*/MBP and *Cnp*/CNP display approximately similar transcript levels in P18–P31 versus P50–P90 MOL and protein abundance levels in P18 versus P75 myelin. On the other hand, *Plp1* transcript abundance in P50–P90 MOL decreased compared to P18–P31 MOL while the abundance of PLP in myelin increased between P18 and P75, although moderately. It has been previously noted that the abundance in myelin of the subunits of the septin filament that stabilizes mature CNS myelin (SEPTIN2, SEPTIN4, SEPTIN7, and SEPTIN8) increases coinciding with the development of the CNS, with the strongest increase being that of SEPTIN4 and the adaptor protein ANLN (Erwig, Patzig, et al., 2019; Patzig et al., 2016). This increase is also manifest in the present proteome dataset (Figure 2c). However, only *Septin4*, *Septin7*, and *Anln* display increased transcript levels in P50–P90 compared
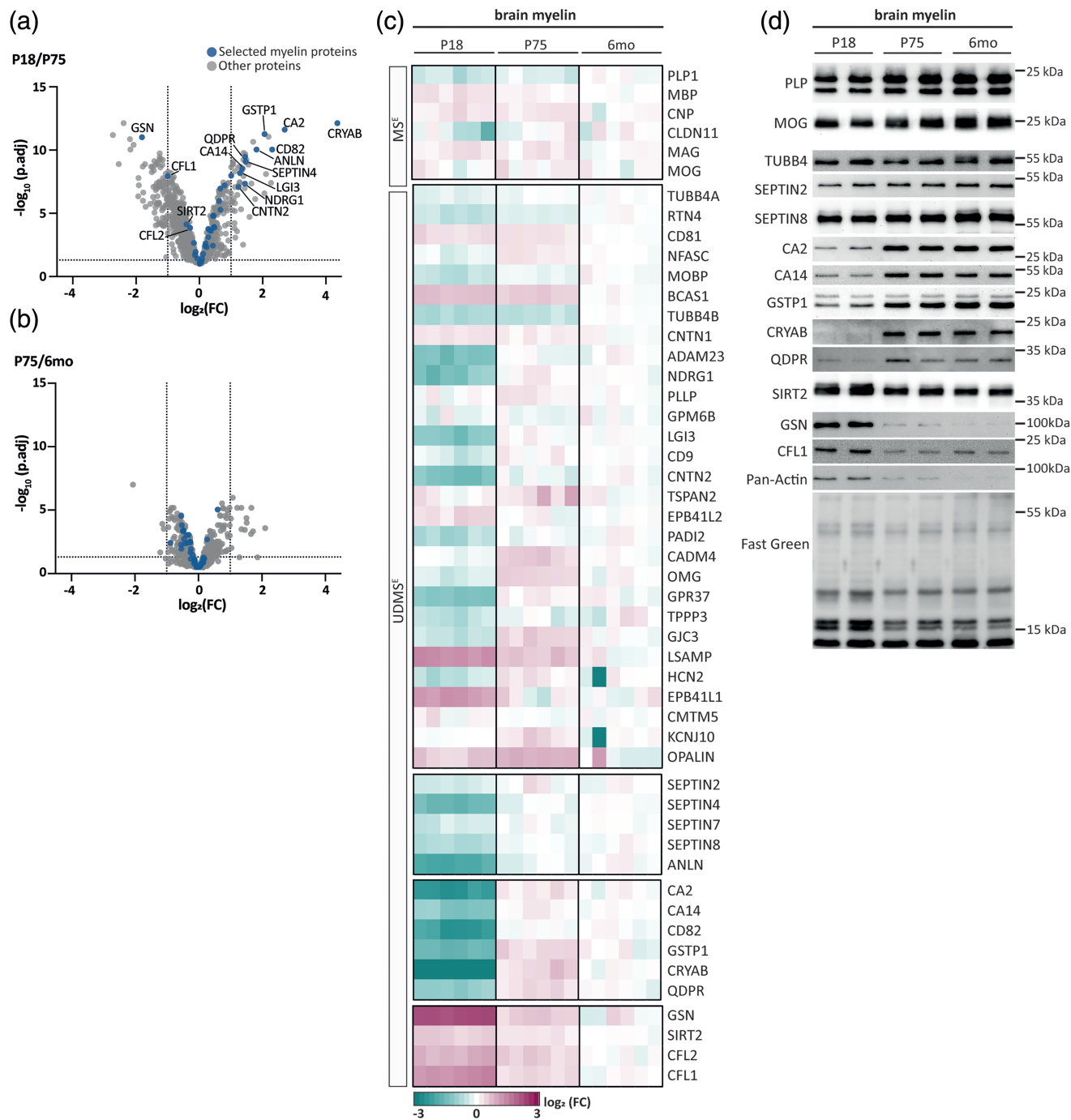
FIGURE 2 Changes of the CNS myelin proteome during postnatal brain maturation. (a, b) Volcano plots comparing the UDMS^E proteome datasets of myelin purified from the brains of mice at P18 and P75 (a), and at P75 and 6 months (b). Protein abundance is plotted as $\log_2$-transformed fold-change (FC) on the x-axis against the $-\log_{10}$-transformed adjusted p-value (p.adj) on the y-axis. Stippled lines respectively indicate a minimal $\log_2$FC of |1.0| (factor >2.0 on normal scale) and a minimal $-\log_{10}$-transformed p.adj-value of 1.301 (p.adj <.05 on normal scale) as significance threshold. $n = 3$ biological replicates were analyzed per group with two technical replicates each. Datapoints highlighted in blue represent known myelin proteins; gray datapoints represent other proteins mass spectrometrically quantified in myelin. Note that the myelin proteome changes considerably between P18 and P75 but remains comparatively similar between P75 and 6 months. For entire dataset see Supplemental Table S1. (c) Heatmap displaying selected known myelin proteins with higher (magenta) or lower (green) abundance in myelin purified from the brains of mice at P18, P75, and 6 months compared to the averaged abundance in myelin at 6 months of age. Heatmap shows three biological replicates per condition with two technical replicates each. Note that myelin maturation coincides with an increase in the abundance of all subunits of the myelin septin filament (SEPTIN2, SEPTIN4, SEPTIN7, SEPTIN8, and ANLN) and multiple proteins (CA2, CA14, CD82, GSTP1, CRYAB, and QDPR) with potentially protective functions, as well as decreased abundance of multiple proteins associated with actin or microtubules (GSN, SIRT2, CFL1, and CFL2). (d) Immunoblot analysis of selected myelin proteins confirms mass spectrometrically quantified abundance changes during myelin maturation. Blot shows $n = 2$ mice per age. Fast green protein staining as loading control.

to P18–P31 MOL, while that of *Septin2* decreased (Supplemental Figure S2). CA2, CA14, CD82, GSTP1, CRYAB, and QDPR also displayed increased protein abundance in P75 versus P18 myelin; however, only *Ca2, Cd82, Gstp1, Cryab,* and *Qdpr* transcript abundance in MOL increased at P18–P31 versus P50–P90, while that of *Ca14* decreased. On the other hand, the abundance of GSN, SIRT2, CFL1, and CFL2 decreased in P75 versus P18 myelin; however, only *Gsn* transcript abundance in MOL decreased at P18–P31 versus P50–P90, while that of *Cfl1* increased. Thus, not all maturation-dependent changes of protein abundance in myelin correlate with a similar trend of the respective mRNA in MOL, at least with the selected conditions.

2.3 | QDPR as a marker for oligodendrocytes and myelin

Considering that QDPR was identified among the proteins of which the abundance in purified myelin markedly increased with maturation (Figure 2c,d) but that its expression has not yet been characterized well, we aimed to confirm its expression in myelin and oligodendrocytes using independent methods. By immunohistochemistry, a previous study (Miyajima et al., 2022) did not detect cells double-immunopositive for QDPR and the astrocyte marker glial fibrillary acidic protein (GFAP) in the corpus callosum, or the serotoninergic neuron marker tryptophan hydroxylase (TPH) in the dorsal raphe nucleus, or the monoaminergic neuron marker tyrosine hydroxylase (TH) in the substantia nigra pars compacta or the locus coeruleus. On the other hand, at least some cells in the striatum were double-immunopositive for QDPR and the oligodendrocyte marker CNP (Miyajima et al., 2022). Notwithstanding that these results were not quantified, they imply that QDPR is expressed in at least some oligodendrocytes in the brain.

We thus asked if expression of *Qdpr* mRNA in oligodendrocytes is also evidenced by an RNA-Seq database of cell types sorted from mouse cortices (GEO dataset GSE52564; Zhang et al., 2014). Indeed, *Qdpr* mRNA was enriched in myelinating oligodendrocytes compared to newly formed oligodendrocytes, and in both of these oligodendroglial stages compared to all other analyzed cell types (oligodendrocyte precursor cells [OPC], endothelial cells, microglia, astrocytes, and neurons) (Figure 3a). For comparison, *Car2* mRNA, encoding the oligodendroglial marker carbonic anhydrase 2 (CA2) (Ghandour et al., 1980), was also enriched in myelinating oligodendrocytes (Figure 3a). However, compared to *Car2* mRNA, *Qdpr* mRNA was enriched to a higher extent in myelinating oligodendrocytes over endothelial cells and astrocytes. *Bcas1* mRNA, encoding brain-enriched myelin associated protein 1 (BCAS1; previously termed breast cancer amplified sequence 1), a marker for newly formed oligodendrocytes (Fard et al., 2017; Kaji et al., 2020), was enriched in newly formed and myelinating oligodendrocytes compared to OPC, and virtually undetectable in other brain cell types (Figure 3a).

To test if human MOL also express *Qdpr* mRNA, we assessed a previously published resource (Gargareta et al., 2022) which included and integrated MOL subset from multiple available scRNA-seq datasets of humans (Grubman et al., 2019; Habib et al., 2017; Jäkel et al., 2019; Lake et al., 2018; Wheeler et al., 2020; Zhou et al., 2020) and mice (Falcão et al., 2018; Marques et al., 2016; Saunders et al., 2018; Wheeler et al., 2020; Ximerakis et al., 2019; Zeisel et al., 2015, 2018). The official gene name of the human ortholog of *Car2* is *CA2*. Indeed, MOL of both mice and humans express *Qdpr* mRNA (Figure 3b). For comparison, *Car2/CA2* and *Bcas1* mRNA are also expressed in MOL of both species (Figure 3b).

We then used immunohistochemistry to compare QDPR-immunopositivity of cell bodies in mouse brains with immunopositivity for either CA2 or BCAS1 (Figure 3c,d). Indeed, a very high proportion of cells (>95%) was double-immunopositive for both QDPR and CA2 in both corpora callosa and cortices (Figure 3c,e). In both CNS regions, a markedly smaller proportion of cells (<5%) was QDPR$^+$/CA2$^-$, and almost no cells (<0.5%) were CA2$^+$/QDPR$^-$. In corpora callosa, a similarly high proportion of cells (93.9%) was double-immunopositive for QDPR and BCAS1; 2.1% of cells were QDPR$^+$/BCAS1$^-$, and 4% of cells were BCAS1$^+$/QDPR$^-$. In cortices, however, the proportion of cells double-immunopositive for both QDPR and BCAS1 was lower (69.3%) while a larger proportion of cells (29.4%) was BCAS1$^+$/QDPR$^-$ (Figure 3d,f), most probably newly formed oligodendrocytes (Figure 3a); 1.3% of cells was QDPR$^+$/BCAS1$^-$. Considering that CA2 and BCAS1, respectively, are established antigenic markers for myelinating and newly formed oligodendrocytes (Fard et al., 2017; Ghandour et al., 1980), this indicates that QDPR-immunohistochemistry detects oligodendrocytes, preferentially at the MOL stage.

To confirm QDPR as a myelin protein with methods independent of mass spectrometry, we first used immunoblotting to assess its abundance in biochemically purified myelin compared to equal amounts of mouse brain homogenate. One band was detected at the expected molecular weight of 26 kDa (Figure 3g). Indeed, QDPR was enriched in the myelin fraction compared to brain lysate, though moderately, as expected for a protein that localizes to both oligodendrocyte cell bodies and myelin sheaths. In comparison, marker proteins largely confined to myelin sheaths (CNP, MBP) were strongly enriched in purified myelin, a marker protein for the oligodendroglial nuclear/cytoplasmic compartment (OLIG2) was reduced in purified myelin, and a marker protein present in both oligodendrocyte cell bodies and myelin sheaths (CA2) was detected with approximately equal band intensity in myelin fractions and brain lysate (Figure 3g).

We then co-immunolabeled QDPR on longitudinal optic nerve sections together with the myelin marker MOG. By confocal microscopy (Figure 3h) we found considerable proximity of the labeling, thereby confirming QDPR as a constituent of CNS myelin. To determine the exact localization of QDPR in myelin we used cryo-immuno electron microscopy of optic nerves dissected from mice. Using antibodies specific for QDPR and protein-A coupled to 10 nm gold particles (Figure 3i), QDPR was readily detectable in the adaxonal, non-compact compartment of CNS myelin (Figure 3i). Together, QDPR emerges as a marker for both oligodendrocyte cell bodies and CNS myelin.

2.4 | Comparing the CNS myelin proteome between male and female mice

To visualize the comparison of the proteome of myelin purified from the brains of male and female mice at P75, we displayed the entire datasets as volcano plot (Figure 4a), as well as selected known myelin proteins in a heatmap (Figure 4b). In agreement with the PCA and Pearson's correlation coefficients (Figure 1e,h), the volcano plot and heatmap did not provide evidence of substantial sex-dependent differences (Figure 4a,b). These mass spectrometric comparisons were
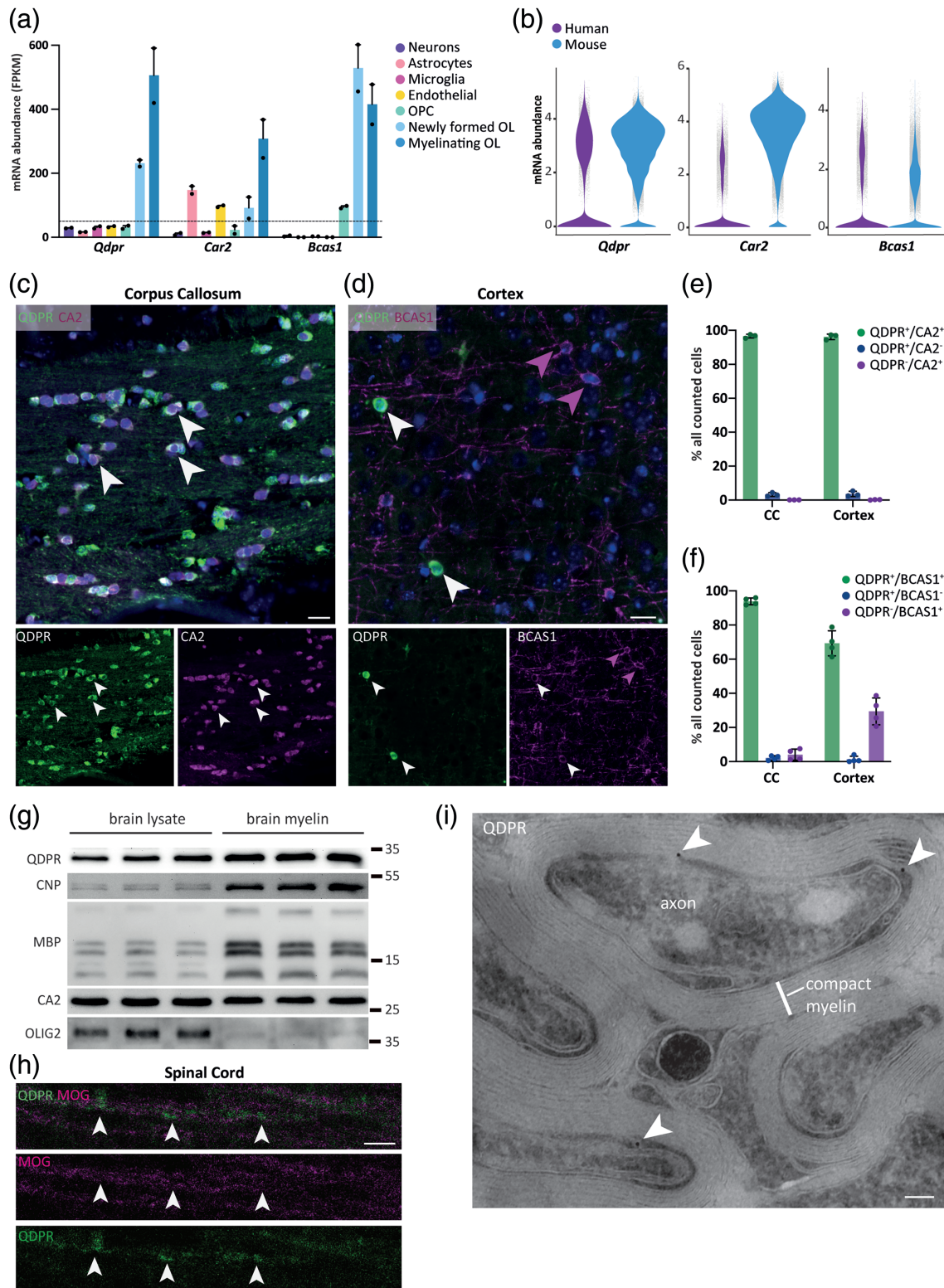

FIGURE 3 Legend on next page.

generally confirmed by immunoblotting of selected of these proteins (Figure 4c). Together, this indicates that the myelin proteome of male and female mice is essentially similar, at least at P75.

2.5 | Comparing the proteome of myelin-enriched fractions from four CNS regions

Finally, we aimed to compare the proteome of myelin purified from four different CNS regions dissected from mice at P75. While assessing the datasets in heatmaps, we noticed that the abundance of most known myelin proteins in the fractions across the CNS regions did not differ extensively (Figure 5a), despite the evident separation of the datasets according to PCA and Pearson's correlation coefficients (Figure 1f,i). Indeed, the most consistent region-dependent difference in abundance of a known myelin protein was the markedly higher abundance of hyperpolarization-activated cyclic nucleotide-gated potassium and sodium channel 2 (HCN2) in myelin purified from spinal cords compared to that of cortices, optic nerves and corpora callosa (Figure 5a). Importantly, a comparatively high level of HCN2 mRNA has been previously recognized (Seeker et al., 2023) as part of a gene set that defines a cluster of oligodendrocytes in the spinal cord of humans (cluster Oligo_F in Seeker et al., 2023). Thus, the comparatively high abundance of HCN2 protein in myelin purified from spinal cords, at least in mice (Figure 5a), correlates with a comparatively high abundance of HCN2 mRNA in spinal cord oligodendrocytes, at least in humans (Seeker et al., 2023).

When further assessing the datasets, we noticed that mitochondrial and synaptic proteins display considerably different abundances across the myelin fractions from the four CNS regions (Figure 5b). Mitochondrial proteins appeared fairly enriched in myelin fractions from the gray matter (cortex) compared to a mixed tract (spinal cord), and in both compared to the white matter (corpus callosum, optic nerve) (Figure 5b), including the mitochondrial-encoded mitochondrial proteins (MTCO1, MTCO2, MTND1, and MTATP8) (Figure 5b). Synaptic proteins were enriched in myelin fractions from the cortex compared to all other CNS regions (Figure 5b). The mass spectrometric comparisons were generally confirmed by immunoblot-detection of myelin, mitochondrial, and synapse marker proteins (Figure 5c,d). The separation of the proteome datasets of myelin fractions from the CNS regions according to PCA and Pearson's correlation coefficients (Figure 1f,i) is thus at least partially affected by a higher fraction of mitochondrial and synaptic membranes in the gray matter, which co-purify with myelin to some extent, most likely due to overlapping floatation properties of the respective membranes in sucrose gradients.

To compare the degree of co-purification of membranes from other cellular structures with myelin fractions derived from different CNS regions we plotted the total PPM according to the UDMS^E dataset of markers for mitochondria, synapses, and known myelin proteins (Figure 5e). Indeed, the total PPM of mitochondrial and synaptic markers in the myelin fractions was more than double in the cortex (42,200 PPM) compared to spinal cord (16,500 PPM), corpus callosum (14,000 PPM) or optic nerve (8000 PPM) (turquoise bars in Figure 5e). On the other hand, the total PPM of known myelin proteins was approximately similar across the CNS regions (magenta bars in Figure 5e). Together, the finding that HCN2 is comparatively abundant in myelin purified from spinal cords implies that regional differences in myelin protein composition exist. Yet, we cannot exclude that the partial co-purification of mitochondrial and synaptic membranes, which display region-dependent abundance, may have masked possible other, more subtle differences in the relative abundance of genuine myelin proteins.

FIGURE 3 Validation of QDPR as a marker for oligodendrocytes and myelin. (a) Abundance of mRNA encoding quinoid dihydropteridine reductase (Qdpr) in cells immunopanned from mouse cortex according to a previously published cell-type specific RNA-Seq dataset (Zhang et al., 2014). Note that Qdpr mRNA is enriched in myelinating oligodendrocytes (MOL) compared to neurons (N), astrocytes (AS), microglia (MG), endothelial cells (EC), oligodendrocyte precursor cells (OPC), and newly formed oligodendrocytes (NFO). For comparison, mRNA abundance of the oligodendrocyte markers Carbonic anhydrase 2 (Car2/CA2) and Brain-enriched myelin-associated protein (Bcas1/BCAS1) was plotted. Mean ± SEM; n = 2; stippled line indicates 40 FPKM (fragments per kilobase of transcript per million mapped reads). (b) Violin plot of Qdpr mRNA abundance in MOL of humans and mice according to previously integrated scRNA-seq data (Gargareta et al., 2022). Each datapoint represents one MOL. Note that Qdpr mRNA is expressed in both mouse and human MOL. (c) Immunohistochemical analysis of coronal brain sections of C57Bl/6N mice at P75 immunolabeled for QDPR (green) and the oligodendrocyte marker CA2 (magenta). Arrowheads point at double-immunopositive cell bodies in the corpus callosum. Image representative of n = 3 mice. Scale bar 20 μm. (d) Immunohistochemical analysis of coronal brain sections of C57Bl/6N mice at P17 immunolabeled for QDPR (green) and the oligodendrocyte marker BCAS1 (magenta). Arrowheads point at double-immunopositive cell bodies in the cortex. Image representative of n = 4 mice. Scale bar 20 μm. (e) Quantitative assessment of QDPR$^+$/CA2$^+$ double-immunopositive cells, QDPR$^+$/CA2$^-$ single-immunopositive cells, and QDPR$^-$/CA2$^+$ single-immunopositive cells on micrographs as in (c). Mean ± SD. Datapoints represent n = 3 individual mice. Note that most QDPR$^+$ cells are also immunopositive for CA2. (f) Quantitative assessment of QDPR$^+$/BCAS1$^+$ double-immunopositive cells, QDPR$^+$/BCAS1$^-$ single-immunopositive cells, and QDPR$^-$/BCAS1$^+$ single-immunopositive cells on micrographs as in (d). Mean ± SD. Datapoints represent n = 3 individual mice. Note that most QDPR$^+$ cells are also immunopositive for BCAS1. (g) Immunoblot analysis of brain lysate and myelin purified from the brains of C57Bl/6N mice at P75. Note that myelin markers (MBP, CNP) are enriched in purified myelin while markers of other cellular sources including oligodendrocyte cell bodies (OLIG2) are reduced. The moderate enrichment of QDPR with myelin purification is thus consistent with localization in both oligodendrocyte cell bodies and myelin. Blot shows n = 3 mice per fraction. (h) Immunohistochemical analysis of longitudinal spinal cord sections of C57Bl/6N mice at age 6 months immunolabeled for QDPR (green) and the myelin marker MOG (magenta). Arrowheads point at double-immunopositive myelin sheaths. Image representative of n = 4 mice. Scale bar 5 μm. (i) Immunodetection of QDPR visualized with 10 nm gold particles (white arrowheads) pointing at gold particles that appear as black puncta on cryosectioned optic nerves of C57Bl/6N mice at age 8 months. Image representative of n = 3 mice. Note that QDPR labeling in axon/myelin-units was mostly confined to the adaxonal myelin compartment. Scale bar 100 nm.

FIGURE 4 The CNS myelin proteome of male and female mice is essentially similar. (a) Volcano plot comparing the UDMS^E proteome datasets of myelin purified from the brains of male and female C57Bl/6N mice at P75. Protein abundance is plotted as log$_2$-transformed fold-change (FC) on the x-axis against the $-\log_{10}$-transformed adjusted p-value (p.adj) on the y-axis. Stippled lines respectively indicate a minimal log$_2$FC of |1.0| (factor >2.0 on normal scale) and a minimal $-\log_{10}$-transformed p. adj-value of 1.301 (p.adj <.05 on normal scale) as significance threshold. Datapoints highlighted in blue represent known myelin proteins; gray datapoints represent other proteins mass spectrometrically quantified in myelin. $n = 3$ biological replicates were analyzed per group with two technical replicates each. Note that male and female mice display essentially similar CNS myelin proteomes. For entire dataset see Supplemental Table S2. (b) Heatmap displaying selected known myelin proteins with higher (magenta) or lower (green) abundance in myelin purified from the brains of female or male mice compared to the averaged abundance in myelin of male mice. Note that the relative abundance of known myelin proteins is essentially similar. Columns represent $n = 3$ biological replicates per group with two technical replicates each. (c) Immunoblot analysis of selected myelin proteins confirms the proteome analysis results. Fast green protein staining as loading control. Blot shows $n = 3$ mice per group.
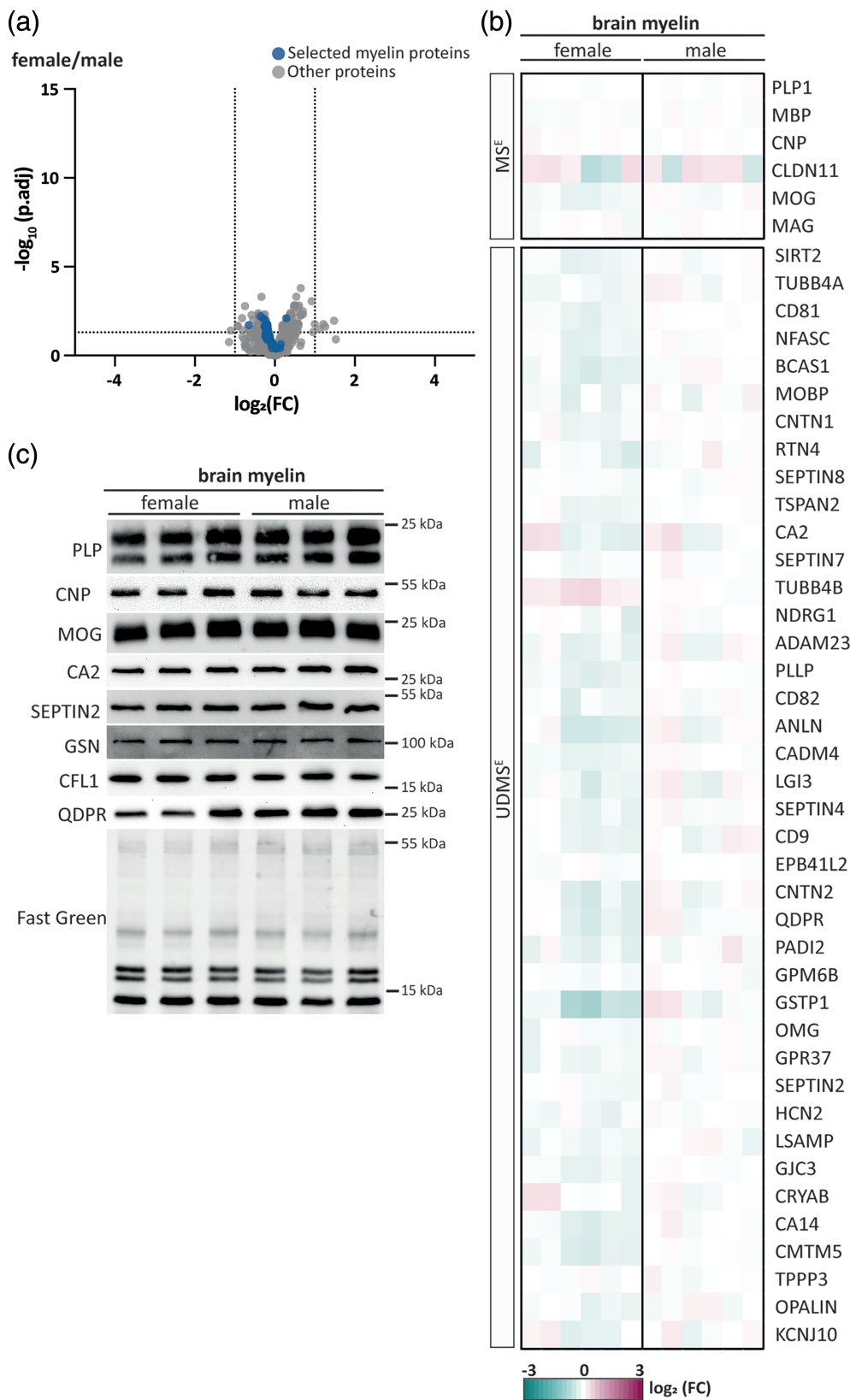
3 | DISCUSSION

Here, we asked to which extent the CNS myelin proteome varies within the same species. To this aim we performed label-free mass spectrometric analysis of myelin-enriched fractions biochemically purified from the CNS of mice. The protein composition of the myelin fractions was compared at three ages, between male and female mice, and across four CNS regions. The approach facilitated the identification of
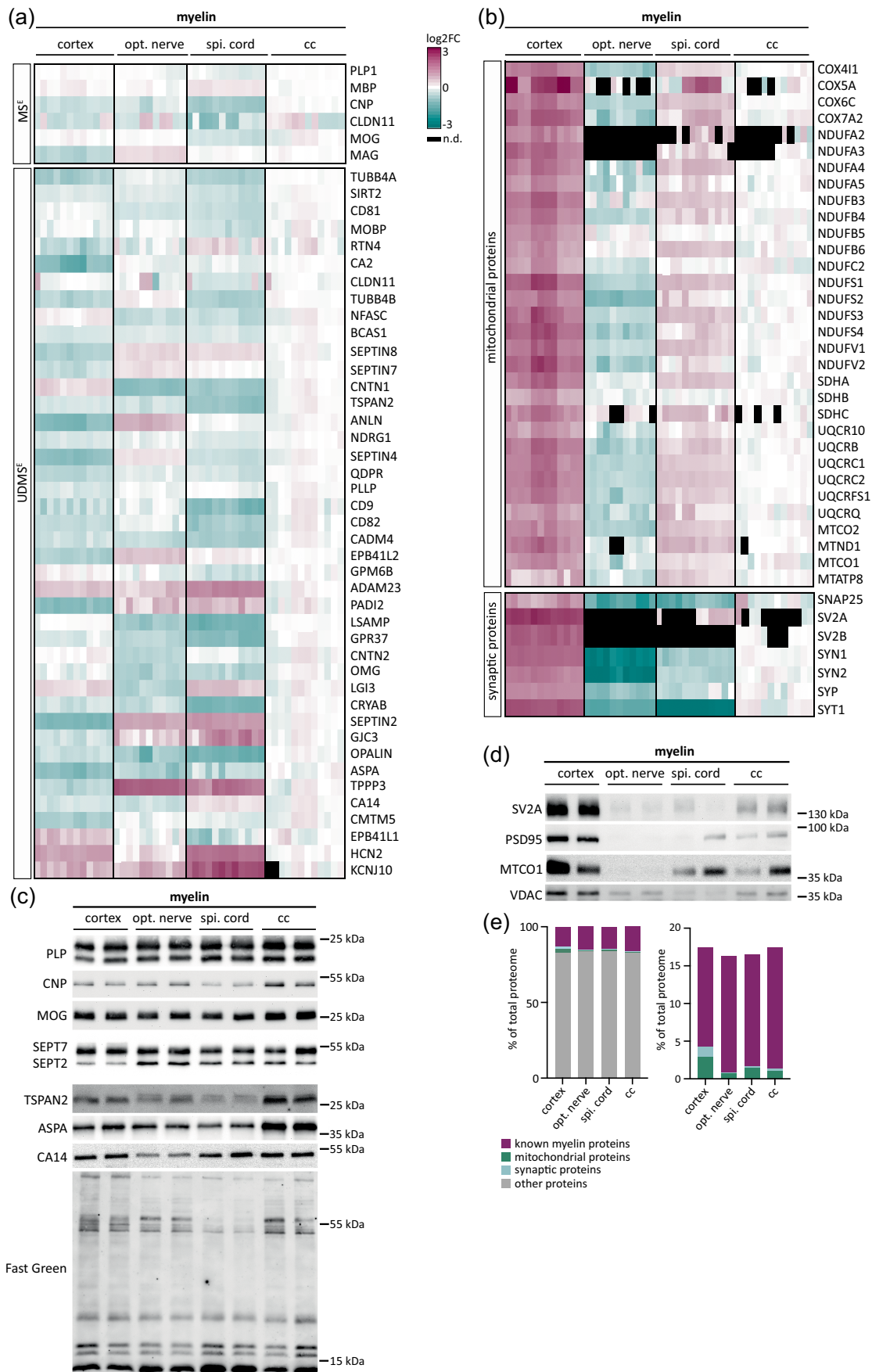
FIGURE 5 Legend on next page.

hundreds of proteins and their simultaneous quantification, thereby gaining information about their relative abundance.

Our data indicate that the abundance of multiple myelin proteins is subject to developmental changes. For example, the abundance in myelin of distinct cytoskeleton-associated proteins linked to actin (CFL1, CFL2, and GSN) or microtubules (SIRT2) decreases during myelin maturation. It is likely that their functions are particularly relevant during active biogenesis of myelin, which involves the depolymerization of actin filaments (Cristobal et al., 2022; Nawaz et al., 2015; Zuchero et al., 2015). It is plausible that—after the developmental compaction of myelin—only a low amount of these proteins remains present in the compartments of myelin that escape compaction. It is of note, however, that the function of oligodendroglial SIRT2 (Ji et al., 2011; Li et al., 2007; Southwood et al., 2007; Werner et al., 2007) is not limited to removing posttranslational modifications from substrate proteins during myelination (Jablonska et al., 2022; Ma et al., 2022). Indeed, SIRT2 is a cargo of oligodendroglial exosomes (Chamberlain et al., 2021; Frühbeis et al., 2020) and upon the transcellular transfer to axons mediates deacetylation of mitochondrial proteins in the latter (Chamberlain et al., 2021); its deficiency in mice causes a late-onset axonopathy (Fourcade et al., 2017). This indicates that a maturation-dependent decrease of the abundance of a protein in myelin does not exclude functional relevance at a later stage.

On the other hand, several proteins display an increase in their abundance during myelin maturation. This is exemplified by QDPR, which catalyzes the NADH-mediated reduction of quinonoid dihydrobiopterin (Kono et al., 2023). Notably, mice lacking QDPR-expression from all cells develop hyperphenylalaninemia and monoamine deficiency in the brain, as well as enhanced fear responses, at least at an age of over 4 months (Miyajima et al., 2022). In humans, homozygous missense, nonsense and frameshift mutations of the QDPR gene cause QDPR-deficiency and hyperphenylalaninemia (Howells et al., 1990; Romstad et al., 2000). We find that QDPR is a highly specific marker for mature oligodendrocytes and myelin. Thus, oligodendrocytes and myelin serve an important QDPR-dependent function in monoamine metabolism in vivo, with relevance for normal behavioral capabilities. The maturation-dependent increase in the abundance of QDPR in myelin is comparable to that of the subunits of septin filaments that assemble in the adaxonal layer to stabilize mature myelin sheaths, thereby enabling normal impulse propagation velocity (Erwig, Patzig,

et al., 2019; Patzig et al., 2016). The maturation-dependent increase in the abundance in myelin of carbonic anhydrases (CA2, CA14) is not surprising when considering the results of enzyme assays in the 1970s that measured the enzymatic activity of carbonic anhydrases in myelin fractions purified from rat brains via two sucrose density gradients and two osmotic shocks (Cammer et al., 1977), essentially similar to the moderately modified protocol used in the present study. Indeed, carbonic anhydrase activity showed a developmental increase, with the largest rise taking place before P60 (Cammer et al., 1977). Together, QDPR, myelin septin filaments, carbonic anhydrases, and other "late" myelin proteins, including the antioxidative glutathione S-transferase-pi1 (GSTP1), the immunomodulatory tetraspanin CD82, and the small heat shock protein crystallin-αB (CRYAB), may be involved in the roles of oligodendrocytes and myelin in preventing CNS pathology (Depp et al., 2023; Nave & Werner, 2014; Stadelmann et al., 2019; van Noort et al., 2010; Wolf et al., 2020) and psychiatric disorder (Haroutunian et al., 2014; Khelfaoui et al., 2024; Nave & Ehrenreich, 2014; Vanes et al., 2020) upon maturation of myelin.

The biogenesis and ultrastructure of myelin require specialized myelin proteins. Interestingly, the abundance of most structural myelin proteins including MBP, CNP, MAG, MOG, plasmolipin (PLLP), tetraspanin-2 (TSPAN2), and chemokine-like factor-like MARVEL transmembrane domain containing protein 5 (CMTM5) remains approximately similar between the ages analyzed here. This may reflect that a particular abundance of a protein in the myelin sheath corresponds to its function as a molecular "building block," independent of the maturational stage. Yet, it is not always straightforward to correlate a protein's abundance and structural function in myelin when considering that many myelin proteins are also required for preserving a healthy CNS, including CNP (Edgar et al., 2009; Lappe-Siefke et al., 2003), MAG (Nguyen et al., 2009; Steyer et al., 2022), TSPAN2 (De Monasterio-Schrader et al., 2013), CMTM5 (Buscham et al., 2022; Zhan et al., 2023), and PLP (Griffiths et al., 1998; Lüders et al., 2017; Saugier-Veber et al., 1994). Indeed, the cholesterol-associated tetraspan PLP is exceptionally abundant in myelin (Gargareta et al., 2022; Jahn et al., 2020) and critical for maintaining both myelin ultrastructure and axonal integrity (Möbius et al., 2008). Interestingly, an experimental reduction of PLP-abundance in myelin by 50% was sufficient to cause both myelin pathology and axonopathy (Lüders et al., 2019). This indicates that not merely the presence of a protein in myelin but also its precise abundance is relevant for a healthy CNS.

FIGURE 5 Comparing the proteome of myelin purified from different CNS regions. (a, b) Heatmap displaying selected myelin proteins (a) as well as mitochondrial and synaptic proteins (b) with higher (magenta) or lower (green) abundance or not detected (black) in myelin-enriched fractions purified from cortex, optic nerve, spinal cord or corpus callosum (cc) dissected from C57Bl/6N mice at P75 compared to the averaged abundance in corpus callosum myelin. Columns represent three biological replicates per group with four technical replicates each. For each biological replicate, the respective CNS regions dissected from three mice were pooled before myelin purification. Note that proteins associated with mitochondria and synapses are strongly enriched in myelin purified from the gray matter (cortex) or a mixed CNS region (spinal cord) compared to the white matter (optic nerve, corpus callosum), indicating that mitochondrial and synaptic membranes partially co-purify with the myelin fraction. For entire dataset see Supplemental Table S3. (c, d) Immunoblot analysis of selected myelin proteins (c) as well as mitochondrial (MTCO1, VDAC) and synaptic proteins (SV2A, PSD95) (d) confirms the higher abundance of synaptic and mitochondrial proteins that co-purify with cortical myelin. Fast Green protein staining as loading control. Blot shows $n = 2$ mice per region. (e) Quantification in parts per million (PPM) of known myelin proteins (magenta), mitochondrial proteins (dark turquoise), synaptic proteins (light turquoise), and other proteins (gray) mass spectrometrically quantified by UDMS[E] in myelin purified from the different CNS regions. Note that mitochondrial and synaptic proteins constitute 4.2% of the total protein in myelin purified from cortex compared with 0.8%–1.7% of the total protein in myelin purified from optic nerve, spinal cord or corpus callosum.

In the 1970s, aiming to discern the protein composition of CNS myelin during postnatal development, myelin was enriched from mouse brains using cesium chloride (CsCl)-gradients, separated by SDS-PAGE, and the comprised proteins were visualized by Fast Green labeling (Morell et al., 1972). Considering that the major bands were constituted by the most abundant myelin proteins (PLP, MBP, and CNP), it was possible to assess changes of their relative abundance (see Figure 8 in Morell et al., 1972). The bands mainly constituted by CNP (labeled W for Wolfgram protein at that time) and two isoforms of MBP (labeled B_S and B_F) remained about equally intense for myelin purified at ages between P15 and P60. Conversely, the band mainly constituted by PLP (labeled P) considerably increased in intensity between P15 and P60 (Morell et al., 1972). Notwithstanding that the present work assessed myelin at P18 and P75, mass spectrometric quantification thus principally confirmed the earlier result. This raises confidence that biochemical analysis of myelin is fairly reproducible across different laboratories, even when using different methods for purification (e.g., CsCl and sucrose gradients), separation (SDS-PAGE and liquid chromatography), and detection (e.g., Fast Green labeling and mass spectrometry). Yet, the mass spectrometric techniques available now are much more powerful than gels when considering that many more proteins can be identified, and quantified with a much higher dynamic range.

A mass spectrometric comparison of the protein composition of female and male CNS myelin was indicated because of previously noted sex-dependent effects, for example in myelination (Harry et al., 1985; Mohamed et al., 2020), Multiple Sclerosis (MS) (Kalincik et al., 2013), and experimental autoimmune encephalomyelitis (EAE) (Alvarez-Sanchez & Dunn, 2023; Hoghooghi et al., 2020). Yet, the present analysis did not reveal sex-dependent differences in the myelin proteome, at least in mice at P75. We note that this finding is in principal agreement with a recent comparison of the transcriptional profiles of oligodendrocytes in humans between females and males (Seeker et al., 2023). This work reported the existence of only few sex-dependent differences, which were mainly owing to X- and Y-chromosome encoded transcripts, the protein products of which are not constituents of the myelin proteome. To the best of our knowledge, thus, there is currently no evidence of sexual dimorphism in myelin protein composition.

When comparing the proteome datasets of myelin purified from different CNS regions, the high abundance of hyperpolarization-activated cyclic nucleotide-gated potassium and sodium channel 2 (HCN2) in spinal cord myelin represented the strongest and most coherent region-dependent difference. Notably, spinal cord oligodendrocytes have been previously noted to express high *HCN2* transcript levels, at least in humans (Seeker et al., 2023). Considering that *Hcn2*-expression enables the formation of particularly long myelin sheaths, at least in mouse brains (Swire et al., 2021), the formation of the especially long myelin sheaths that the spinal cord comprises corresponds well with the high abundance of HCN2 in spinal cord myelin, possible species- or region-dependent differences notwithstanding.

However, in this experiment it also became evident that mitochondrial and synaptic proteins are identified at higher abundance in the myelin fraction from the cortex compared to those of spinal cord, corpus callosum, and optic nerve. The identification of mitochondrial

and synaptic proteins in myelin-enriched fractions is not unexpected because mitochondria and synaptic vesicles partly co-purify with myelin membranes. Importantly, mitochondrial and synaptic membranes are strongly reduced in the myelin fractions compared to brain lysates; however, they are not removed completely (Jahn et al., 2013; Thakurela et al., 2016). Vice versa, proteome datasets of mitochondria-enriched fractions (Graham et al., 2017; Pagliarini et al., 2008) or synaptic vesicles (Takamori et al., 2006; Taoufiq et al., 2020) purified from mammalian CNS tissue commonly comprise canonical myelin proteins including PLP, MBP, MOBP, and MAG. In proteomic approaches to mitochondrial or synaptic fractions, thus, myelin membranes may be rightly viewed as contaminants. Partial co-purification occurs probably due to floatation properties in sucrose or Percoll gradients that are not sufficiently different as to allow complete separation.

The identification in myelin fractions of the mitochondrial-encoded mitochondrial proteins MTND1, MTCO1, MTCO2, and MTATP8, respectively subunits of complexes I, IV, and V, supports the view that entire mitochondria are not totally separated away during the procedure of myelin purification and are thus comprised in the myelin-enriched fraction as contaminant, rather than nuclear-encoded mitochondrial proteins expressed in oligodendrocytes being mis-routed to be incorporated into myelin membranes. Indeed, a small number of intact-appearing mitochondria can be observed when assessing myelin fractions purified from whole brains by transmission electron microscopy (Werner et al., 2007). This view is also in agreement with a prior consideration of energy balances, which concluded that it is very unlikely that a (hypothetical) respiratory chain localized in myelin membranes could generate ATP similar to mitochondria (Harris & Attwell, 2013). The enrichment of synaptic and mitochondrial proteins in myelin fractions from the gray matter (cortex), compared to a mixed tract (spinal cord) or white matter tracts (optic nerve, corpus callosum), is thus probably owing to a higher fraction of synaptic and mitochondrial membranes in gray compared to white matter, correlating with the presence of more synapses and synaptic mitochondria in the gray matter (Harris et al., 2012; Rangaraju et al., 2014). However, both synapse-like components (Hughes & Appel, 2019; Marques et al., 2016; Micu et al., 2018) and a few mitochondria (Rinholm et al., 2016) have been observed in oligodendrocytes and mature myelin sheaths, and are also unlikely to be entirely separated away from myelin membranes during myelin purification. It thus remains a question for future investigation if the mitochondrial and synaptic proteins identified in the myelin fraction originate from mitochondria and synaptic elements derived from neurons, oligodendrocytes, or other cell types in the CNS. Together, potential masking effects of differentially co-purified mitochondrial and synaptic membranes on region-dependent differences in myelin protein abundance can only be excluded once more efficient protocols have become available that allow the separation of myelin from other subcellular membrane structures.

3.1 | Limitations of the study

Notwithstanding that omics analysis of individual myelin sheaths, or of all myelin sheaths extended by the same oligodendrocyte, may

become technically possible in the future, the methodology available at this time only allows bulk analysis of myelin fractions biochemically purified from tissue lysates. As for each biochemical fraction, this will inevitably include some degree of partial co-purification of other cellular structures, as evidenced by the myelin fraction comprising up to 5% of mitochondrial and synaptic proteins among the total PPM. Considering that the degree of co-purification varies between CNS regions, it appears crucial to design each experiment using well-controlled conditions. In the present work we have thus not compared each condition with all other conditions. Instead, as far as technically possible, each quantitative proteome analysis experiment was on myelin fractions purified in the same rotor run, samples prepared and mass spectrometry performed in parallel, all under the same conditions. In consequence, we cannot formally exclude that differences in myelin protein composition may exist that did not become evident here, for example, a difference that depends on both sex and CNS region exclusively at younger or older age. Future technical developments may enable the identification of such differences.

4 | CONCLUSION

Myelination of the CNS is a continuous process but has been subdivided into consecutive steps, that is, the establishment of glia-axonal contacts, polarization of oligodendroglial processes, myelin membrane growth coinciding with the association of major myelin proteins and lipids, longitudinal and radial sheath expansion (i.e., wrapping), spatial segregation of sheaths at the nodes of Ranvier, and finally the compaction of adjacent myelin layers (Nave & Werner, 2014). Our data imply that the protein composition of myelin matures as a late stage of myelination. The high abundance in spinal cord myelin of HCN2, which facilitates the formation of particularly long myelin sheaths (Swire et al., 2021), correlates well with the presence of especially long myelin sheaths in the spinal cord. On the other hand, sexual dimorphism of myelin protein composition was not evident.

5 | METHODS

5.1 | Mice

For comparisons across CNS regions and development, male C57Bl/6N mice were bred in the animal facility of the Max Planck Institute for Multidisciplinary Sciences (MPI-NAT); CNS tissue was dissected at the indicated ages. According to the German Animal Welfare Law (Tierschutzgesetz der Bundesrepublik Deutschland, TierSchG) and the regulation about animals used in experiments, dated 11th of Aug 2021 (Tierschutz-Versuchstierverordnung, TierSchVersV), an animal welfare officer and an animal welfare committee are established for the institute. For procedures of sacrificing rodents for subsequent preparation of tissue, all regulations given in the Animal Welfare Law §4 (TierSchG §4) are followed. Since sacrificing of animals is not an experiment on animals according to TierSchG §7 Abs. 2 Satz 3, no specific authorization is required. The animal

facility at the MPI-NAT is registered according to TierSchG §11 Abs. 1. For sex-dependent comparison, male and female C57Bl/6J mice were housed at the animal facility of the Icahn School of Medicine and bred according to approved IACUC protocols; brains were harvested at postnatal day 75.

5.2 | Myelin purification

A lightweight membrane fraction enriched for myelin was purified from the CNS of C57Bl/6N mice following an established protocol (Erwig, Hesse, et al., 2019) based on two sucrose density gradient centrifugation steps and osmotic shocks. Myelin accumulates between layers of 0.32 and 0.85 M sucrose.

5.3 | Proteome analysis

In-solution digestion of myelin proteins by filter-aided sample preparation (FASP) (Erwig, Hesse, et al., 2019) and LC–MS-analysis by different MS^E-type data-independent acquisition (DIA) mass spectrometry approaches was performed as recently established for mouse PNS and CNS (Jahn et al., 2020; Siems et al., 2020) and human CNS (Gargareta et al., 2022) myelin. Briefly, protein fractions corresponding to 10 μg myelin protein were dissolved in lysis buffer (1% ASB-14, 7 M urea, 2 M thiourea, 10 mM DTT, 0.1 M Tris pH 8.5) and processed according to a CHAPS-based FASP protocol in centrifugal filter units (30 kDa MWCO, Merck Millipore). After removal of the detergents, protein alkylation with iodoacetamide, and buffer exchange to digestion buffer (50 mM ammonium bicarbonate (ABC), 10% acetonitrile), proteins were digested overnight at 37°C with 400 ng trypsin. Tryptic peptides were recovered by centrifugation and extracted with 40 μL of 50 mM ABC and 40 μL of 1% trifluoroacetic acid (TFA), respectively. For quantification according to the TOP3 approach (Silva et al., 2006), combined flow-through were spiked with 10 fmol/μL of yeast enolase-1 tryptic digest (Waters Corporation) and directly subjected to LC–MS-analysis.

Tryptic peptides were separated by nanoscale reversed-phase UPLC and mass spectrometrically analyzed on a quadrupole time-of-flight mass spectrometer with ion mobility option (Synapt G2-S, Waters Corporation) as recently described in detail (Gargareta et al., 2022; Jahn et al., 2020; Siems et al., 2020). Briefly, the samples were first analyzed in the ion mobility-enhanced DIA mode with drift time-specific collision energies referred to as UDMS^E (Distler et al., 2014) to maximize proteome coverage, and subsequently re-run in a data acquisition mode without ion mobility separation of peptides (referred to as MS^E) to ensure the correct quantification of exceptionally abundant myelin proteins. Continuum LC–MS data were processed using Waters ProteinLynx Global Server (PLGS) and searched against a custom database compiled by adding the sequence information for yeast enolase 1 and porcine trypsin to the UniProtKB/Swiss-Prot mouse proteome (release 2021-03, 17,082 entries) and by appending the reversed sequence of each entry to enable the determination of false discovery rate (FDR) set to 1% threshold.

For post-identification analysis including TOP3 quantification of proteins and for the detection of significant changes in protein

abundance by moderated *t*-statistics, the freely available software ISOQuant (Distler et al., 2014) and the Bioconductor R package "limma" were used as described (Jahn et al., 2020; Siems et al., 2020). Only proteins represented by at least two peptides (minimum length seven amino acids, score ≥5.5, identified in at least two runs) were quantified as parts per million (PPM), that is, the relative amount (w/w) of each protein in respect to the sum over all detected proteins. FDR for both peptides and proteins was set to 1% threshold and at least one unique peptide was required. Proteins identified as contaminants from blood (albumin, hemoglobin) or skin/hair cells (keratins) were removed and potential outlier proteins were revised by inspecting the quality of peptide identification, quantification and distribution between protein isoforms. Filtered protein lists were subjected to statistical analysis with "limma" and correction of *p*-values for multiple comparisons was performed according to Benjamini and Hochberg (1995) using the function *p*.adjust built-in in R. For data visualization of pairwise comparisons by volcano plots, corrected *p*-values (*p*.adj) were plotted against fold-change after −log10 and log2 transformation, respectively. For visualization of entire proteome datasets, Pearson's correlation coefficients derived from log2-transformed PPM abundance values were clustered and visualized with the tool heatmap.2 contained in the R package "gplots." Only pairwise complete observations were considered to reduce the influence of missing values on clustering behavior. Similarly, principal component analyses (PCA) were based on complete cases, that is, proteins quantified in each replicate of all groups of the respective experiment to prevent potential clustering effects of missing values. The PCA of the three ages was calculated from 661 complete cases out of a total of 1019 proteins; the PCA of the four CNS regions was calculated from 789 complete cases out of 1164 proteins, and the PCA of the two sexes was calculated from 779 complete cases out of 804 proteins. Proteomic data were visualized in volcano plots and heatmaps generated using Microsoft Excel and GraphPad Prism10 as previously described (Gargareta et al., 2022; Siems et al., 2020).

5.4 | Silver staining and immunoblotting of gels

SDS-PAGE, silver staining of gels and immunoblotting were performed as previously described (Buscham et al., 2022; Schardt et al., 2009). Protein concentration was determined using the DC Protein assay kit (Bio-Rad, Hercules, CA) and samples diluted in 1× SDS buffer and 5% dithiothreitol. After adding loading buffer, the samples were heated at 40°C for 10 min and separated on a SDS-PAGE for 50–60 min using the Bio-Rad system. After blotting, quality of the transfer and samples was analyses by total protein staining using Fast Green solution. Membranes were briefly washed in Fast Green washing solution and incubated for 5 min in 1× Fast Green solution followed by two washing steps. Fast Green signals were detected with the deepRed excitation Filter (670 nm) using the ChemoStar fluorescent imager (INTAS Science Imaging Instruments GmbH, Germany). Primary antibodies were specific for proteolipid protein (PLP A431, provided by Martin Jung, 1:5000), myelin oligodendrocyte glycoprotein (MOG clone 8-18C5,

provided by Christopher Linington, 1:1000), tubulin beta-4 (TUBB4, Sigma #SAB2102603; 1:1000), SEPTIN2 (ProteinTech #11397-1-AP; 1:500), SEPTIN7 (IBL JP18991; 1:5000), SEPTIN8 (ProteinTech #11769-1-AP; 1:2500), carbonic anhydrase 2 (CA2, provided by Said Ghandour, 1:1000), carbonic anhydrase 14 (CA14, ProteinTech #13736-1-AP, 1:1000), glutathione S transferase (GSTP1, ProteinTech #15902-1-AP, 1:1000), alpha-crystallin-b (CRYAB, ProteinTech #15808-1-AP, 1:500), dihydropteridine reductase (QDPR, ProteinTech #14904-1-AP, 1:1000), sirtuin-2 (SIRT2, Abcam #ab67299, 1:500), gelsolin (GSN, Cell Signaling #D9W8Y, 1:1000), cofilin (CFL1, Abcam #ab42824, 1:1000), myelin basic protein (MBP, Meschkat et al., 2022, 1:2000), 2′,3′-cyclic-nucleotide 3′-phosphodiesterase (CNP, Sigma #SAB1405637, 1:1000), tetraspanin-2 (TSPAN2, ProteinTech #20463-1-AP, 1:500), aspartoacylase (ASPA, ProteinTech #13244-1-AP 1:500), synaptic vesicle glycoprotein 2A (SV2A, Novus Biologicals #NBP1-82964, 1:1000), post synaptic density 95 kDa (PSD95, Affinity BioReagents #MA1-046, 1:1000), cytochrome c oxidase subunit 1 (MTCO1, Abcam #ab14705, 1:2500), voltage-dependent anion-selective channel protein (VDAC, Rockland #600-401-882). Appropriate secondary anti-mouse, anti-rabbit, and anti-rat antibodies conjugated to HRP were from Dianova (HRP goat anti-mouse #115-035-003, 1:10,000, HRP goat anti-rabbit #111-035-003, 1:10,000, HRP goat anti-rat #112-035-167, 1:10,000). Immunoblots were developed with the LightningR Plus-ECL solutions (Western Lightning Plus, Perkin Elmer, Waltham, MA) or the Super Signal West Femto Maximum Sensitivity Substrate (Thermo Fisher Scientific, Rockford, IL) and detected with the Intas ChemoCam system (INTAS Science Imaging Instruments GmbH, Göttingen, Germany). Exposure time was set to 1–6 min and raw images were inverted using the ChemaStarTS software (INTAS Science Imaging Instruments GmbH, Göttingen, Germany) and cropped in Adobe® Illustrator 2022.

5.5 | Immunohistochemistry and analysis of imaging data

For Immunohistochemistry, mice were transcardially perfused with Hank's buffered salt solution (HBSS) and 4% paraformaldehyde (PFA) in 0.1 M phosphate buffer (PB) for tissue fixation. The tissue was dissected and post-fixed with 4% PFA in 0.1 M PB overnight and stored in PBS until further processing. Fixed brain samples were dehydrated and embedded in paraffin using an automated embedding system (Leica Microsystems) as described (Depp et al., 2023). Samples were embedded into paraffin blocks, cut into 5 μm coronal sections, collected on microscope slides and dried overnight. Before immunolabeling slides were deparaffinized and rehydrated. For antigen retrieval the deparaffinized sections were incubated in Tris/EDTA buffer (pH 9.0) followed by 10 min incubation in boiling Tris/EDTA buffer. Samples were cooled to RT, rinsed with PBS (2× 5 min) and permeabilized in 0.1% Triton X-100 in PBS (15 min). To block unspecific antibody binding sites, sections were incubated in blocking buffer (10% goat serum in PBS; 1 h at RT) followed by incubation with

respective primary antibodies in antibody solution (5% goat serum with PBS; overnight at 4°C). Primary antibodies were specific for CA2 (Abcam #ab124687, 1:1000), QDPR (ProteinTech #14904-1-AP, 1:300), BCAS1 (Synaptic Systems #445003, 1:300), proteolipid protein (PLP A431, provided by Martin Jung, 1:5000), myelin oligodendrocyte glycoprotein (MOG clone8-18C5, provided by Christopher Linington, 1:1000). Slides were briefly rinsed in PBS (3× 5 min) followed by incubation with respective fluorescent secondary antibodies and DAPI (Thermo-Fisher, 1:50,000) diluted in 10% goat serum in PBS (1 h at RT). Secondary antibodies were donkey anti-rat Alexa 555 (Invitrogen, 1:1000), donkey anti-rabbit Alexa 555 (Invitrogen, 1:1000), donkey anti-rabbit DyLight 650 (Invitrogen, 1:1000), and donkey anti-guinea pig DyLight 650 (Invitrogen, 1:1000). Sections were washed with PBS (2× 5 min) and incubated with DAPI (1:10,000; 5 min, RT). After a final washing step with PBS (1× 5 min) the sections were mounted in Aqua-Poly/Mount (Polysciences) and stored at 4°C. Fluorescent sections were imaged using an Observer Z1/Z2 microscopes (Zeiss) with a Colibri 5 LED light source (630, 555, 475, 385 nm excitation) the Zeiss Filter sets: 96 HE BFP, 90 HE DAPI/GFP/Cy3/Cy5, 38 GFP, 43 DsRed, 50 Cy5, and an Axiocam MrM at 20× or 40× magnification or using a Leica SP8 Lightning confocal microscope with an adjustable white-light laser at 63× magnification. If required, stitching of single images was performed post acquisition using ZEN. To display the images, channels were assigned pseudo-colors and adjusted using FIJI. Numbers of oligodendrocytes immunopositive for CA2, QDPR, and BCAS1 were manually quantified using the cell counter function in FIJI.

5.6 | Cryo-immuno electron microscopy

Immuno-gold labeling of optic nerve cryosections was essentially performed as described (Werner et al., 2007). Briefly, optic nerves were dissected from 8 months old wildtype C57Bl/6N mice and subsequently fixed in Immuno-Karlsson-Schultz fixative (0.25% glutaraldehyde, 4% formaldehyde in 0.1 M phosphate buffer containing 0.5% NaCl) overnight at 4°C. Afterwards the nerves were cut into short pieces, stained with toluidine blue and embedded in gelatin (10%) blocks. To protect the tissue before cryo-sectioning, the blocks were infiltrated with sucrose in 0.1 M phosphate buffer overnight (4°C). Gelatin blocks were mounted on aluminum pins and frozen in liquid nitrogen. Cryo-sections of 50 nm were cut using a Diatome Diamond knife, cryo-immuno 2.0 mm (Diatome, Switzerland) on a Leica UC6 ultramicrotome with FC6 cryochamber (Leica, Vienna, Austria). The sections were collected and transferred to carbon coated grids and stored at 4°C. Before antibody labeling, the sections were washed in PBS (3× 2 min) followed by two washing steps in PBS with glycine (0.1%) and incubation in 1% BSA in PBS (3 min) to block unspecific antibody binding sides. Primary antibodies were specific for QDPR (ProteinTech #14904-1-AP) and diluted (1:200) in 1% BSA in PBS and applied for 1 h. Following the incubation with primary antibodies, the sections were washed and incubated with the respective Immuno-gold coupled secondary antibody (1:40). Sections were washed again (5× 2 min, PBS) and fixed with 1% glutaraldehyde in PBS (5 min). To enhance the contrast, the sections were stained with uranyl acetate and methylcellulose-uranyl acetate, and sections were imaged with a LEO EM912 Omega (Zeiss, Germany).

5.7 | mRNA expression analysis

Publicly available scRNA-seq dataset GSE775330 (Marques et al., 2016) was used for differential gene expression (DGE) analysis. The dataset was previously processed using Seurat R package version 3.1.4 as described (Gargareta et al., 2022). Briefly, data were normalized with LogNormalize, followed by the identification of the 2000 most variable features, and data scaling. All six clusters identified as myelinating oligodendrocytes (MOL) by (Marques et al., 2016) were subset for DGE using Seurat R package version 4.3.2 to compare expression in MOL between juvenile mice (P18–P31) and adult mice (P50–P90). DGE was calculated using the FindMarkers function (non-parametric Wilcoxon rank sum test) with min.pct = 0.1, adjusted p-values *p < .05; **p < .01; ***p < .001, and a minimum average log2FC of ±0.25. Violin plots were generated using ggplot2 with the previously scaled data.

CONFLICT OF INTEREST STATEMENT

The authors declare no competing interests.

DATA AVAILABILITY STATEMENT

All relevant data are included in the main article or supplemental files. The mass spectrometry proteomics data have been deposited to the

ProteomeXchange Consortium via the PRIDE (Perez-Riverol et al., 2019) partner repository at https://www.ebi.ac.uk/pride/ with dataset identifier PXD053062.

ORCID

Sophie B. Siems https://orcid.org/0000-0002-7760-2507
Vasiliki-Ilya Gargareta https://orcid.org/0000-0002-6673-0714
Leonie C. Schadt https://orcid.org/0009-0000-9792-4354
Vinicius Daguano Gastaldi https://orcid.org/0000-0002-6249-6035
Ramona B. Jung https://orcid.org/0009-0000-4095-1773
Lars Piepkorn https://orcid.org/0009-0004-6165-5307
Patrizia Casaccia https://orcid.org/0000-0002-4785-9264
Ting Sun https://orcid.org/0000-0002-7104-7215
Olaf Jahn https://orcid.org/0000-0002-3397-8924
Hauke B. Werner https://orcid.org/0000-0002-7710-5738

REFERENCES

Alvarez-Sanchez, N., & Dunn, S. E. (2023). Immune cell contributors to the female sex bias in multiple sclerosis and experimental autoimmune encephalomyelitis. *Current Topics in Behavioral Neurosciences*, *62*, 333–373.

Autilio, L. A., Norton, W. T., & Terry, R. D. (1964). The preparation and some properties of purified myelin from the central nervous system. *Journal of Neurochemistry*, *11*, 17–27.

Benjamini, Y., & Hochberg, Y. (1995). Controlling the false discovery rate: A practical and powerful approach to multiple testing. *Journal of the Royal Statistical Society Series B: Statistical Methodology*, *57*, 289–300.

Buscham, T. J., Eichel-Vogel, M. A., Steyer, A. M., Jahn, O., Strenzke, N., Dardawal, R., Memhave, T. R., Siems, S. B., Müller, C., Meschkat, M., Sun, T., Ruhwedel, T., Möbius, W., Krämer-Albers, E.-M., Boretius, S., Nave, K.-A., & Werner, H. B. (2022). Progressive axonopathy when oligodendrocytes lack the myelin protein CMTM5. *eLife*, *11*, e75523.

Cammer, W., Bieler, L., Fredman, T., & Norton, W. T. (1977). Quantitation of myelin carbonic anhydrase-development and subfractionation of rat brain myelin and comparison with myelin from other species. *Brain Research*, *138*, 17–28.

Chamberlain, K. A., Huang, N., Xie, Y., LiCausi, F., Li, S., Li, Y., & Sheng, Z.-H. (2021). Oligodendrocytes enhance axonal energy metabolism by deacetylation of mitochondrial proteins through transcellular delivery of SIRT2. *Neuron*, *109*, 3456–3472.e8.

Cristobal, C. D., Wang, C.-Y., Zuo, Z., Smith, J. A., Lindeke-Myers, A., Bellen, H. J., & Lee, H. K. (2022). Daam2 regulates myelin structure and the oligodendrocyte actin cytoskeleton through Rac1 and gelsolin. *The Journal of Neuroscience*, *42*, 1679–1691.

De Monasterio-Schrader, P., Patzig, J., Möbius, W., Barrette, B., Wagner, T. L., Kusch, K., Edgar, J. M., Brophy, P. J., & Werner, H. B. (2013). Uncoupling of neuroinflammation from axonal degeneration in mice lacking the myelin protein tetraspanin-2. *Glia*, *61*, 1832–1847.

Depp, C., Sun, T., Sasmita, A. O., Spieth, L., Berghoff, S. A., Nazarenko, T., Overhoff, K., Steixner-Kumar, A. A., Subramanian, S., Arinrad, S., Ruhwedel, T., Möbius, W., Göbbels, S., Saher, G., Werner, H. B., Damkou, A., Zampar, S., Wirths, O., Thalmann, M., ... Nave, K.-A. (2023). Myelin dysfunction drives amyloid-β deposition in models of Alzheimer's disease. *Nature*, *618*, 349–357.

Distler, U., Kuharev, J., Navarro, P., Levin, Y., Schild, H., & Tenzer, S. (2014). Drift time-specific collision energies enable deep-coverage data-independent acquisition proteomics. *Nature Methods*, *11*, 167–170.

Distler, U., Kuharev, J., Navarro, P., & Tenzer, S. (2016). Label-free quantification in ion mobility–enhanced data-independent acquisition proteomics. *Nature Protocols*, *11*, 795–812.

Djannatian, M., Timmler, S., Arends, M., Luckner, M., Weil, M. T., Alexopoulos, I., Snaidero, N., Schmid, B., Misgeld, T., Möbius, W., Schifferer, M., Peles, E., & Simons, M. (2019). Two adhesive systems cooperatively regulate axon ensheathment and myelin growth in the CNS. *Nature Communications*, *10*, 4794.

Edgar, J. M., McLaughlin, M., Werner, H. B., McCulloch, M. C., Barrie, J. A., Brown, A., Faichney, A. B., Snaidero, N., Nave, K. A., & Griffiths, I. R. (2009). Early ultrastructural defects of axons and axon-glia junctions in mice lacking expression of Cnp1. *Glia*, *57*, 1815–1824.

Elazar, N., Vainshtein, A., Golan, N., Vijayaragavan, B., Schaeren-Wiemers, N., Eshed-Eisenbach, Y., & Peles, E. (2019). Axoglial adhesion by Cadm4 regulates CNS myelination. *Neuron*, *101*, 224–231.

Elazar, N., Vainshtein, A., Rechav, K., Tsoory, M., Eshed-Eisenbach, Y., & Peles, E. (2019). Coordinated internodal and paranodal adhesion controls accurate myelination by oligodendrocytes. *Journal of Cell Biology*, *218*, 2887–2895.

Erwig, M. S., Hesse, D., Jung, R. B., Uecker, M., Kusch, K., Tenzer, S., Jahn, O., & Werner, H. B. (2019). Myelin: Methods for purification and proteome analysis. *Methods in Molecular Biology*, *1936*, 37–63.

Erwig, M. S., Patzig, J., Steyer, A. M., Dibaj, P., Heilmann, M., Heilmann, I., Jung, R. B., Kusch, K., Möbius, W., Jahn, O., Nave, K.-A., & Werner, H. B. (2019). Anillin facilitates septin assembly to prevent pathological outfoldings of central nervous system myelin. *eLife*, *8*, e43888.

Falcão, A. M., van Bruggen, D., Marques, S., Meijer, M., Jäkel, S., Agirre, E., Samudyata, F. E. M., Vanichkina, D. P., Ffrench-Constant, C., Williams, A., Guerreiro-Cacais, A. O., & Castelo-Branco, G. (2018). Disease-specific oligodendrocyte lineage cells arise in multiple sclerosis. *Nature Medicine*, *24*, 1837–1844.

Fard, M. K., Van Der Meer, F., Sánchez, P., Cantuti-Castelvetri, L., Mandad, S., Jäkel, S., Fornasiero, E. F., Schmitt, S., Ehrlich, M., Starost, L., Kuhlmann, T., Sergiou, C., Schultz, V., Wrzos, C., Brück, W., Urlaub, H., Dimou, L., Stadelmann, C., & Simons, M. (2017). BCAS1 expression defines a population of early myelinating oligodendrocytes in multiple sclerosis lesions. *Science Translational Medicine*, *9*, eaam7816.

Fourcade, S., Morató, L., Parameswaran, J., Ruiz, M., Ruiz-Cortés, T., Jové, M., Naudí, A., Martínez-Redondo, P., Dierssen, M., Ferrer, I., Villarroya, F., Pamplona, R., Vaquero, A., Portero-Otín, M., & Pujol, A. (2017). Loss of SIRT2 leads to axonal degeneration and locomotor disability associated with redox and energy imbalance. *Aging Cell*, *16*, 1404–1413.

Frühbeis, C., Kuo-Elsner, W. P., Müller, C., Barth, K., Peris, L., Tenzer, S., Möbius, W., Werner, H. B., Nave, K.-A., Fröhlich, D., & Krämer-Albers, E.-M. (2020). Oligodendrocytes support axonal transport and maintenance via exosome secretion. *PLoS Biology*, *18*, e3000621.

Fünfschilling, U., Supplie, L. M., Mahad, D., Boretius, S., Saab, A. S., Edgar, J., Brinkmann, B. G., Kassmann, C. M., Tzvetanova, I. D., Möbius, W., Diaz, F., Meijer, D., Suter, U., Hamprecht, B., Sereda, M. W., Moraes, C. T., Frahm, J., Goebbels, S., & Nave, K.-A. (2012). Glycolytic oligodendrocytes maintain myelin and long-term axonal integrity. *Nature*, *485*, 517–521.

Gargareta, V., Reuschenbach, J., Siems, S. B., Sun, T., Piepkorn, L., Mangana, C., Späte, E., Goebbels, S., Huitinga, I., Möbius, W., Nave, K.-A., Jahn, O., & Werner, H. B. (2022). Conservation and divergence of myelin proteome and oligodendrocyte transcriptome profiles between humans and mice. *eLife*, *11*, e77019.

Ghandour, M. S., Vincendon, G., Gombos, G., Limozin, N., Filippi, D., Dalmasso, C., & Laurent, G. (1980). Carbonic anhydrase and oligodendroglia in developing rat cerebellum: A biochemical and immunohistological study. *Developmental Biology*, *77*, 73–83.

Gopalakrishnan, G., Awasthi, A., Belkaid, W., De Faria, O., Liazoghli, D., Colman, D. R., & Dhaunchak, A. S. (2013). Lipidome and proteome map of myelin membranes. *Journal of Neuroscience Research*, *91*, 321–334.

Graham, L. C., Eaton, S. L., Brunton, P. J., Atrih, A., Smith, C., Lamont, D. J., Gillingwater, T. H., Pennetta, G., Skehel, P., & Wishart, T. M. (2017). Proteomic profiling of neuronal mitochondria reveals modulators of synaptic architecture. *Molecular Neurodegeneration*, 12, 77.

Griffiths, I., Klugmann, M., Anderson, T., Yool, D., Thomson, C., Schwab, M. H., Schneider, A., Zimmermann, F., McCulloch, M., Nadon, N., & Nave, K. A. (1998). Axonal swellings and degeneration in mice lacking the major proteolipid of myelin. *Science*, 280, 1610–1613.

Grubman, A., Chew, G., Ouyang, J. F., Sun, G., Choo, X. Y., McLean, C., Simmons, R. K., Buckberry, S., Vargas-Landin, D. B., Poppe, D., Pflueger, J., Lister, R., Rackham, O. J. L., Petretto, E., & Polo, J. M. (2019). A single-cell atlas of entorhinal cortex from individuals with Alzheimer's disease reveals cell-type-specific gene expression regulation. *Nature Neuroscience*, 22, 2087–2097.

Habib, N., Avraham-Davidi, I., Basu, A., Burks, T., Shekhar, K., Hofree, M., Choudhury, S. R., Aguet, F., Gelfand, E., Ardlie, K., Weitz, D. A., Rozenblatt-Rosen, O., Zhang, F., & Regev, A. (2017). Massively parallel single-nucleus RNA-seq with DroNc-seq. *Nature Methods*, 14, 955–958.

Haley, J. E., Samuels, F. G., & Ledeen, R. W. (1981). Study of myelin purity in relation to axonal contaminants. *Cellular and Molecular Neurobiology*, 1, 175–187.

Haroutunian, V., Katsel, P., Roussos, P., Davis, K. L., Altshuler, L. L., & Bartzokis, G. (2014). Myelination, oligodendrocytes, and serious mental illness. *Glia*, 62, 1856–1877.

Harris, J. J., & Attwell, D. (2013). Is myelin a mitochondrion? *Journal of Cerebral Blood Flow and Metabolism*, 33, 33–36.

Harris, J. J., Jolivet, R., & Attwell, D. (2012). Synaptic energy use and supply. *Neuron*, 75, 762–777.

Harry, G. J., Toews, A. D., Krigman, M. R., & Morell, P. (1985). The effect of lead toxicity and milk deprivation of myelination in the rat. *Toxicology and Applied Pharmacology*, 77, 458–464.

Hartline, D. K., & Colman, D. R. (2007). Rapid conduction and the evolution of giant axons and myelinated fibers. *Current Biology*, 17, R29–R35.

Hoghooghi, V., Palmer, A. L., Frederick, A., Jiang, Y., Merkens, J. E., Balakrishnan, A., Finlay, T. M., Grubb, A., Levy, E., Gordon, P., Jirik, F. R., Nguyen, M. D., Schuurmans, C., Visser, F., Dunn, S. E., & Ousman, S. S. (2020). Cystatin C plays a sex-dependent detrimental role in experimental autoimmune encephalomyelitis. *Cell Reports*, 33, 108236.

Howells, D. W., Forrest, S. M., Dahl, H. H., & Cotton, R. G. (1990). Insertion of an extra codon for threonine is a cause of dihydropteridine reductase deficiency. *American Journal of Human Genetics*, 47, 279–285.

Hughes, A. N., & Appel, B. (2019). Oligodendrocytes express synaptic proteins that modulate myelin sheath formation. *Nature Communications*, 10, 4125.

Jablonska, B., Adams, K. L., Kratimenos, P., Li, Z., Strickland, E., Haydar, T. F., Kusch, K., Nave, K.-A., & Gallo, V. (2022). Sirt2 promotes white matter oligodendrogenesis during development and in models of neonatal hypoxia. *Nature Communications*, 13, 4771.

Jahn, O., Siems, S. B., Kusch, K., Hesse, D., Jung, R. B., Liepold, T., Uecker, M., Sun, T., & Werner, H. B. (2020). The CNS myelin proteome: Deep profile and persistence after post-mortem delay. *Frontiers in Cellular Neuroscience*, 14, 239.

Jahn, O., Tenzer, S., Bartsch, N., Patzig, J., & Werner, H. B. (2013). Myelin proteome analysis: Methods and implications for the myelin cytoskeleton. *NeuroMethods*, 79, 335.

Jäkel, S., Agirre, E., Mendanha Falcão, A., van Bruggen, D., Lee, K. W., Knuesel, I., Malhotra, D., Ffrench-Constant, C., Williams, A., & Castelo-Branco, G. (2019). Altered human oligodendrocyte heterogeneity in multiple sclerosis. *Nature*, 566, 543–547.

Ji, S., Doucette, J. R., & Nazarali, A. J. (2011). Sirt2 is a novel in vivo downstream target of Nkx2.2 and enhances oligodendroglial cell differentiation. *Journal of Molecular Cell Biology*, 3, 351–359.

Joseph, S., Vingill, S., Jahn, O., Fledrich, R., Werner, H. B., Katona, I., Möbius, W., Mitkovski, M., Huang, Y., Weis, J., Sereda, M. W., Schulz, J. B., Nave, K.-A., & Stegmüller, J. (2019). Myelinating glia-specific deletion of Fbxo7 in mice triggers axonal degeneration in the central nervous system together with peripheral neuropathy. *The Journal of Neuroscience*, 39, 5606–5626.

Kaji, S., Maki, T., Ueda, J., Ishimoto, T., Inoue, Y., Yasuda, K., Sawamura, M., Hikawa, R., Ayaki, T., Yamakado, H., & Takahashi, R. (2020). BCAS1-positive immature oligodendrocytes are affected by the α-synuclein-induced pathology of multiple system atrophy. *Acta Neuropathologica Communications*, 8, 120.

Kalincik, T., Vivek, V., Jokubaitis, V., Lechner-Scott, J., Trojano, M., Izquierdo, G., Lugaresi, A., Grand'maison, F., Hupperts, R., Oreja-Guevara, C., Bergamaschi, R., Iuliano, G., Alroughani, R., Van Pesch, V., Amato, M. P., Slee, M., Verheul, F., Fernandez-Bolanos, R., Fiol, M., … MSBase Study Group. (2013). Sex as a determinant of relapse incidence and progressive course of multiple sclerosis. *Brain*, 136, 3609–3617.

Kapell, H., Fazio, L., Dyckow, J., Schwarz, S., Cruz-Herranz, A., Mayer, C., Campos, J., D'Este, E., Möbius, W., Cordano, C., Pröbstel, A.-K., Gharagozloo, M., Zulji, A., Narayanan Naik, V., Delank, A., Cerina, M., Müntefering, T., Lerma-Martin, C., Sonner, J. K., … Schirmer, L. (2023). Neuron-oligodendrocyte potassium shuttling at nodes of Ranvier protects against inflammatory demyelination. *The Journal of Clinical Investigation*, 133, e164223.

Kassmann, C. M., Lappe-Siefke, C., Baes, M., Brügger, B., Mildner, A., Werner, H. B., Natt, O., Michaelis, T., Prinz, M., Frahm, J., & Nave, K. A. (2007). Axonal loss and neuroinflammation caused by peroxisome-deficient oligodendrocytes. *Nature Genetics*, 39, 969–976.

Khelfaoui, H., Ibaceta-Gonzalez, C., & Angulo, M. C. (2024). Functional myelin in cognition and neurodevelopmental disorders. *Cellular and Molecular Life Sciences*, 81, 181.

Kono, H., Hara, S., Furuta, T., & Ichinose, H. (2023). Binding profile of quinonoid-dihydrobiopterin to quinonoid-dihydropteridine reductase examined by in silico and in vitro analyses. *Journal of Biochemistry*, 174, 441–450.

Korey, S. R., Orchen, M., & Brotz, M. (1958). Studies of white matter. I. Chemical constitution and respiration of neuroglial and myelin enriched fractions of white matter. *Journal of Neuropathology and Experimental Neurology*, 17, 430–438.

Lake, B. B., Chen, S., Sos, B. C., Fan, J., Kaeser, G. E., Yung, Y. C., Duong, T. E., Gao, D., Chun, J., Kharchenko, P. V., & Zhang, K. (2018). Integrative single-cell analysis of transcriptional and epigenetic states in the human adult brain. *Nature Biotechnology*, 36, 70–80.

Lappe-Siefke, C., Goebbels, S., Gravel, M., Nicksch, E., Lee, J., Braun, P. E., Griffiths, I. R., & Nave, K.-A. (2003). Disruption of Cnp1 uncouples oligodendroglial functions in axonal support and myelination. *Nature Genetics*, 33, 366–374.

Lee, Y., Morrison, B. M., Li, Y., Lengacher, S., Farah, M. H., Hoffman, P. N., Liu, Y., Tsingalia, A., Jin, L., Zhang, P.-W., Pellerin, L., Magistretti, P. J., & Rothstein, J. D. (2012). Oligodendroglia metabolically support axons and contribute to neurodegeneration. *Nature*, 487, 443–448.

Li, W., Zhang, B., Tang, J., Cao, Q., Wu, Y., Wu, C., Guo, J., Ling, E.-A., & Liang, F. (2007). Sirtuin 2, a mammalian homolog of yeast silent information regulator-2 longevity regulator, is an oligodendroglial protein that decelerates cell differentiation through deacetylating alpha-tubulin. *The Journal of Neuroscience*, 27, 2606–2616.

Looser, Z. J., Faik, Z., Ravotto, L., Zanker, H. S., Jung, R. B., Werner, H. B., Ruhwedel, T., Möbius, W., Bergles, D. E., Barros, L. F., Nave, K.-A., Weber, B., & Saab, A. S. (2024). Oligodendrocyte–axon metabolic coupling is mediated by extracellular K+ and maintains axonal health. *Nature Neuroscience*, 27, 433–448.

Louie, A. Y., Kim, J. S., Drnevich, J., Dibaeinia, P., Koito, H., Sinha, S., McKim, D. B., Soto-Diaz, K., Nowak, R. A., Das, A., & Steelman, A. J. (2023). Influenza a virus infection disrupts oligodendrocyte homeostasis and alters the myelin lipidome in the adult mouse. *Journal of Neuroinflammation*, 20, 190.

Lüders, K. A., Nessler, S., Kusch, K., Patzig, J., Jung, R. B., Möbius, W., Nave, K. A., & Werner, H. B. (2019). Maintenance of high proteolipid protein level in adult central nervous system myelin is required to preserve the integrity of myelin and axons. *Glia*, 67, 634–649.

Lüders, K. A., Patzig, J., Simons, M., Nave, K. A., & Werner, H. B. (2017). Genetic dissection of oligodendroglial and neuronal Plp1 function in a novel mouse model of spastic paraplegia type 2. *Glia*, 65, 1762–1776.

Ma, X.-R., Zhu, X., Xiao, Y., Gu, H.-M., Zheng, S.-S., Li, L., Wang, F., Dong, Z.-J., Wang, D.-X., Wu, Y., Yang, C., Jiang, W., Yao, K., Yin, Y., Zhang, Y., Peng, C., Gao, L., Meng, Z., Hu, Z., … Zhao, J.-W. (2022). Restoring nuclear entry of Sirtuin 2 in oligodendrocyte progenitor cells promotes remyelination during ageing. *Nature Communications*, 13, 1225.

Magno-Sumbilla, C., & Campagnoni, A. T. (1977). Factors affecting the electrophoretic analysis of myelin proteins: Application to changes occurring during brain development. *Brain Research*, 126, 131–148.

Manrique-Hoyos, N., Jürgens, T., Grønborg, M., Kreutzfeldt, M., Schedensack, M., Kuhlmann, T., Schrick, C., Brück, W., Urlaub, H., Simons, M., & Merkler, D. (2012). Late motor decline after accomplished remyelination: Impact for progressive multiple sclerosis. *Annals of Neurology*, 71, 227–244.

Marques, S., Zeisel, A., Codeluppi, S., van Bruggen, D., Mendanha Falcao, A., Xiao, L., Li, H., Haring, M., Hochgerner, H., Romanov, R. A., Gyllborg, D., Munoz-Manchado, A. B., La Manno, G., Lonnerberg, P., Floriddia, E. M., Rezayee, F., Ernfors, P., Arenas, E., Hjerling-Leffler, J., … Castelo-Branco, G. (2016). Oligodendrocyte heterogeneity in the mouse juvenile and adult central nervous system. *Science*, 352, 1326–1329.

Marshall-Phelps, K. L. H., Kegel, L., Baraban, M., Ruhwedel, T., Almeida, R. G., Rubio-Brotons, M., Klingseisen, A., Benito-Kwiecinski, S. K., Early, J. J., Bin, J. M., Suminaite, D., Livesey, M. R., Möbius, W., Poole, R. J., & Lyons, D. A. (2020). Neuronal activity disrupts myelinated axon integrity in the absence of NKCC1b. *Journal of Cell Biology*, 219, e201909022.

Meschkat, M., Steyer, A. M., Weil, M.-T., Kusch, K., Jahn, O., Piepkorn, L., Agüi-Gonzalez, P., Phan, N. T. N., Ruhwedel, T., Sadowski, B., Rizzoli, S. O., Werner, H. B., Ehrenreich, H., Nave, K.-A., & Möbius, W. (2022). White matter integrity in mice requires continuous myelin synthesis at the inner tongue. *Nature Communications*, 13, 1163.

Micu, I., Plemel, J. R., Caprariello, A. V., Nave, K.-A., & Stys, P. K. (2018). Axo-myelinic neurotransmission: A novel mode of cell signalling in the central nervous system. *Nature Reviews. Neuroscience*, 19, 49–58.

Miyajima, K., Sudo, Y., Sanechika, S., Hara, Y., Horiguchi, M., Xu, F., Suzuki, M., Hara, S., Tanda, K., Inoue, K., Takada, M., Yoshioka, N., Takebayashi, H., Mori-Kojima, M., Sugimoto, M., Sumi-Ichinose, C., Kondo, K., Takao, K., Miyakawa, T., & Ichinose, H. (2022). Perturbation of monoamine metabolism and enhanced fear responses in mice defective in the regeneration of tetrahydrobiopterin. *Journal of Neurochemistry*, 161, 129–145.

Möbius, W., Patzig, J., Nave, K. A., & Werner, H. B. (2008). Phylogeny of proteolipid proteins: Divergence, constraints, and the evolution of novel functions in myelination and neuroprotection. *Neuron Glia Biology*, 4, 111–127.

Mohamed, E., Paisley, C. E., Meyer, L. C., Bigbee, J. W., & Sato-Bigbee, C. (2020). Endogenous opioid peptides and brain development: Endomorphin-1 and Nociceptin play a sex-specific role in the control of oligodendrocyte maturation and brain myelination. *Glia*, 68, 1513–1530.

Morell, P., Greenfield, S., Costantino-Ceccarini, E., & Wisniewski, H. (1972). Changes in the protein composition of mouse brain myelin during development. *Journal of Neurochemistry*, 19, 2545–2554.

Mukherjee, C., Kling, T., Russo, B., Miebach, K., Kess, E., Schifferer, M., Pedro, L. D., Weikert, U., Fard, M. K., Kannaiyan, N., Rossner, M., Aicher, M. L., Goebbels, S., Nave, K. A., Krämer-Albers, E. M., Schneider, A., & Simons, M. (2020). Oligodendrocytes provide antioxidant defense function for neurons by secreting ferritin heavy chain. *Cell Metabolism*, 32, 259–272.

Nave, K.-A., & Ehrenreich, H. (2014). Myelination and oligodendrocyte functions in psychiatric diseases. *JAMA Psychiatry*, 71, 582–584.

Nave, K.-A., & Werner, H. B. (2014). Myelination of the nervous system: Mechanisms and functions. *Annual Review of Cell and Developmental Biology*, 30, 503–533.

Nawaz, S., Sánchez, P., Schmitt, S., Snaidero, N., Mitkovski, M., Velte, C., Brückner, B. R., Alexopoulos, I., Czopka, T., Jung, S. Y., Rhee, J. S., Janshoff, A., Witke, W., Schaap, I. A. T., Lyons, D. A., & Simons, M. (2015). Actin filament turnover drives leading edge growth during myelin sheath formation in the central nervous system. *Developmental Cell*, 34, 139–151.

Nguyen, T., Mehta, N. R., Conant, K., Kim, K. J., Jones, M., Calabresi, P. A., Melli, G., Hoke, A., Schnaar, R. L., Ming, G. L., Song, H., Keswani, S. C., & Griffin, J. W. (2009). Axonal protective effects of the myelin-associated glycoprotein. *Journal of Neuroscience*, 29, 630–637.

Norton, W. T., & Poduslo, S. E. (1973). Myelination in rat brain: Method of myelin isolation. *Journal of Neurochemistry*, 21, 749–757.

Pagliarini, D. J., Calvo, S. E., Chang, B., Sheth, S. A., Vafai, S. B., Ong, S.-E., Walford, G. A., Sugiana, C., Boneh, A., Chen, W. K., Hill, D. E., Vidal, M., Evans, J. G., Thorburn, D. R., Carr, S. A., & Mootha, V. K. (2008). A mitochondrial protein compendium elucidates complex I disease biology. *Cell*, 134, 112–123.

Patzig, J., Erwig, M. S., Tenzer, S., Kusch, K., Dibaj, P., Möbius, W., Goebbels, S., Schaeren-Wiemers, N., Nave, K. A., & Werner, H. B. (2016). Septin/anillin filaments scaffold central nervous system myelin to accelerate nerve conduction. *eLife*, 5, e17119.

Perez-Riverol, Y., Csordas, A., Bai, J., Bernal-Llinares, M., Hewapathirana, S., Kundu, D. J., Inuganti, A., Griss, J., Mayer, G., Eisenacher, M., Pérez, E., Uszkoreit, J., Pfeuffer, J., Sachsenberg, T., Yilmaz, Ş., Tiwary, S., Cox, J., Audain, E., Walzer, M., … Vizcaíno, J. A. (2019). The PRIDE database and related tools and resources in 2019: Improving support for quantification data. *Nucleic Acids Research*, 47, D442–D450.

Rangaraju, V., Calloway, N., & Ryan, T. A. (2014). Activity-driven local ATP synthesis is required for synaptic function. *Cell*, 156, 825–835.

Rinholm, J. E., Vervaeke, K., Tadross, M. R., Tkachuk, A. N., Kopek, B. G., Brown, T. A., Bergersen, L. H., & Clayton, D. A. (2016). Movement and structure of mitochondria in oligodendrocytes and their myelin sheaths. *Glia*, 64, 810–825.

Romstad, A., Kalkanoğlu, H. S., Coşkun, T., Demirkol, M., Tokatli, A., Dursun, A., Baykal, T., Ozalp, I., Guldberg, P., & Güttler, F. (2000). Molecular analysis of 16 Turkish families with DHPR deficiency using denaturing gradient gel electrophoresis (DGGE). *Human Genetics*, 107, 546–553.

Saugier-Veber, P., Munnich, A., Bonneau, D., Rozet, J. M., le Merrer, M., Gil, R., & Boespflug-Tanguy, O. (1994). X-linked spastic paraplegia and Pelizaeus-Merzbacher disease are allelic disorders at the proteolipid protein locus. *Nature Genetics*, 6, 257–262.

Saunders, A., Macosko, E. Z., Wysoker, A., Goldman, M., Krienen, F. M., de Rivera, H., Bien, E., Baum, M., Bortolin, L., Wang, S., Goeva, A., Nemesh, J., Kamitaki, N., Brumbaugh, S., Kulp, D., & McCarroll, S. A. (2018). Molecular diversity and specializations among the cells of the adult mouse brain. *Cell*, 174, 1015–1030.e16.

Schardt, A., Brinkmann, B. G., Mitkovski, M., Sereda, M. W., Werner, H. B., & Nave, K.-A. (2009). The SNARE protein SNAP-29 interacts with the GTPase Rab3A: Implications for membrane trafficking in myelinating glia. *Journal of Neuroscience Research*, 87, 3465–3479.

Seeker, L. A., Bestard-Cuche, N., Jäkel, S., Kazakou, N.-L., Bøstrand, S. M. K., Wagstaff, L. J., Cholewa-Waclaw, J., Kilpatrick, A. M., Van Bruggen, D., Kabbe, M., Baldivia Pohl, F., Moslehi, Z., Henderson, N. C., Vallejos, C. A., La Manno, G., Castelo-Branco, G., & Williams, A. (2023). Brain matters: Unveiling the distinct contributions of region, age, and sex to glia diversity and CNS function. *Acta Neuropathologica Communications*, 11, 84.

Siems, S. B., Jahn, O., Eichel, M. A., Kannaiyan, N., Wu, L. M. N., Sherman, D. L., Kusch, K., Hesse, D., Jung, R. B., Fledrich, R., Sereda, M. W., Rossner, M. J., Brophy, P. J., & Werner, H. B. (2020). Proteome profile of peripheral myelin in healthy mice and in a neuropathy model. *eLife*, 9, e51406.

Siems, S. B., Jahn, O., Hoodless, L. J., Jung, R. B., Hesse, D., Möbius, W., Czopka, T., & Werner, H. B. (2021). Proteome profile of myelin in the zebrafish Brain. *Frontiers in Cell and Development Biology*, 9, 640169.

Silva, J. C., Gorenstein, M. V., Li, G.-Z., Vissers, J. P. C., & Geromanos, S. J. (2006). Absolute quantification of proteins by LCMS E. *Molecular & Cellular Proteomics*, 5, 144–156.

Southwood, C. M., Peppi, M., Dryden, S., Tainsky, M. A., & Gow, A. (2007). Microtubule deacetylases, SirT2 and HDAC6, in the nervous system. *Neurochemical Research*, 32, 187–195.

Späte, E., Zhou, B., Sun, T., Kusch, K., Asadollahi, E., Siems, S. B., Depp, C., Werner, H. B., Saher, G., Hirrlinger, J., Möbius, W., Nave, K., & Goebbels, S. (2024). Downregulated expression of lactate dehydrogenase in adult oligodendrocytes and its implication for the transfer of glycolysis products to axons. *Glia*, 72, 1374–1391.

Stadelmann, C., Timmler, S., Barrantes-Freer, A., & Simons, M. (2019). Myelin in the central nervous system: Structure, function, and pathology. *Physiological Reviews*, 99, 1381–1431.

Steyer, A. M., Buscham, T. J., Lorenz, C., Hümmert, S., Eichel-Vogel, M. A., Schadt, L. C., Edgar, J. M., Köster, S., Möbius, W., Nave, K.-A., & Werner, H. B. (2022). Focused ion beam-scanning electron microscopy links pathological myelin outfoldings to axonal changes in mice lacking Plp1 or mag. *Glia*, 71, 509–523.

Swire, M., Assinck, P., McNaughton, P. A., Lyons, D. A., Ffrench-Constant, C., & Livesey, M. R. (2021). Oligodendrocyte HCN2 channels regulate myelin sheath length. *The Journal of Neuroscience*, 41, 7954–7964.

Takamori, S., Holt, M., Stenius, K., Lemke, E. A., Grønborg, M., Riedel, D., Urlaub, H., Schenck, S., Brügger, B., Ringler, P., Müller, S. A., Rammner, B., Gräter, F., Hub, J. S., De Groot, B. L., Mieskes, G., Moriyama, Y., Klingauf, J., Grubmüller, H., ... Jahn, R. (2006). Molecular anatomy of a trafficking organelle. *Cell*, 127, 831–846.

Taoufiq, Z., Ninov, M., Villar-Briones, A., Wang, H.-Y., Sasaki, T., Roy, M. C., Beauchain, F., Mori, Y., Yoshida, T., Takamori, S., Jahn, R., & Takahashi, T. (2020). Hidden proteome of synaptic vesicles in the mammalian brain. *Proceedings of the National Academy of Sciences of the United States of America*, 117, 33586–33596.

Tasaki, I. (1939). The electro-saltatory transmission of the nerve impulse and the effect of narcosis upon the nerve fiber. *American Journal of Physiology-Legacy Content*, 127, 211–227.

Taylor, C. M., Marta, C. B., Claycomb, R. J., Han, D. K., Rasband, M. N., Coetzee, T., & Pfeiffer, S. E. (2004). Proteomic mapping provides powerful insights into functional myelin biology. *Proceedings of the National Academy of Sciences of the United States of America*, 101, 4643–4648.

Thakurela, S., Garding, A., Jung, R. B., Müller, C., Goebbels, S., White, R., Werner, H. B., & Tiwari, V. K. (2016). The transcriptome of mouse central nervous system myelin. *Scientific Reports*, 6, 25828.

van Noort, J. M., Bsibsi, M., Gerritsen, W. H., van der Valk, P., Bajramovic, J. J., Steinman, L., & Amor, S. (2010). Alphab-crystallin is a target for adaptive immune responses and a trigger of innate responses in preactive multiple sclerosis lesions. *Journal of Neuropathology and Experimental Neurology*, 69, 694–703.

Vanes, L. D., Moutoussis, M., Ziegler, G., Goodyer, I. M., Fonagy, P., Jones, P. B., Bullmore, E. T., NSPN Consortium, & Dolan, R. J. (2020). White matter tract myelin maturation and its association with general psychopathology in adolescence and early adulthood. *Human Brain Mapping*, 41, 827–839.

Vanrobaeys, F., Van Coster, R., Dhondt, G., Devreese, B., & Van Beeumen, J. (2005). Profiling of myelin proteins by 2D-gel electrophoresis and multidimensional liquid chromatography coupled to MALDI TOF-TOF mass spectrometry. *Journal of Proteome Research*, 4, 2283–2293.

Werner, H. B., Kuhlmann, K., Shen, S., Uecker, M., Schardt, A., Dimova, K., Orfaniotou, F., Dhaunchak, A., Brinkmann, B. G., Mobius, W., Guarente, L., Casaccia-Bonnefil, P., Jahn, O., & Nave, K.-A. (2007). Proteolipid protein is required for transport of Sirtuin 2 into CNS myelin. *Journal of Neuroscience*, 27, 7717–7730.

Wheeler, M. A., Clark, I. C., Tjon, E. C., Li, Z., Zandee, S. E. J., Couturier, C. P., Watson, B. R., Scalisi, G., Alkwai, S., Rothhammer, V., Rotem, A., Heyman, J. A., Thaploo, S., Sanmarco, L. M., Ragoussis, J., Weitz, D. A., Petrecca, K., Moffitt, J. R., Becher, B., ... Quintana, F. J. (2020). MAFG-driven astrocytes promote CNS inflammation. *Nature*, 578, 593–599.

Wolf, N. I., Ffrench-Constant, C., & van der Knaap, M. S. (2020). Hypomyelinating leukodystrophies—Unravelling myelin biology. *Nature Reviews Neurology*, 17, 88–103.

Ximerakis, M., Lipnick, S. L., Innes, B. T., Simmons, S. K., Adiconis, X., Dionne, D., Mayweather, B. A., Nguyen, L., Niziolek, Z., Ozek, C., Butty, V. L., Isserlin, R., Buchanan, S. M., Levine, S. S., Regev, A., Bader, G. D., Levin, J. Z., & Rubin, L. L. (2019). Single-cell transcriptomic profiling of the aging mouse brain. *Nature Neuroscience*, 22, 1696–1708.

Zeisel, A., Hochgerner, H., Lönnerberg, P., Johnsson, A., Memic, F., van der Zwan, J., Häring, M., Braun, E., Borm, L. E., La Manno, G., Codeluppi, S., Furlan, A., Lee, K., Skene, N., Harris, K. D., Hjerling-Leffler, J., Arenas, E., Ernfors, P., Marklund, U., & Linnarsson, S. (2018). Molecular architecture of the mouse nervous system. *Cell*, 174, 999–1014.e22.

Zeisel, A., Moz-Manchado, A. B., Codeluppi, S., Lönnerberg, P., Manno, G. L., Juréus, A., Marques, S., Munguba, H., He, L., Betsholtz, C., Rolny, C., Castelo-Branco, G., Hjerling-Leffler, J., & Linnarsson, S. (2015). Cell types in the mouse cortex and hippocampus revealed by single-cell RNA-seq. *Science*, 347, 1138–1142.

Zhan, J., Gao, Y., Heinig, L., Beecken, M., Huo, Y., Zhang, W., Wang, P., Wei, T., Tian, R., Han, W., Yu, A. C. H., Kipp, M., & Kaddatz, H. (2023). Loss of the novel myelin protein CMTM5 in multiple sclerosis lesions and its involvement in oligodendroglial stress responses. *Cells*, 12, 2085.

Zhang, Y., Chen, K., Sloan, S. A., Bennett, M. L., Scholze, A. R., O'Keeffe, S., Phatnani, H. P., Guarnieri, P., Caneda, C., Ruderisch, N., Deng, S., Liddelow, S. A., Zhang, C., Daneman, R., Maniatis, T., Barres, B. A., & Wu, J. Q. (2014). An RNA-sequencing transcriptome and splicing database of glia, neurons, and vascular cells of the cerebral cortex. *Journal of Neuroscience*, 34, 11929–11947.

Zhou, Y., Song, W. M., Andhey, P. S., Swain, A., Levy, T., Miller, K. R., Poliani, P. L., Cominelli, M., Grover, S., Gilfillan, S., Cella, M., Ulland, T. K., Zaitsev, K., Miyashita, A., Ikeuchi, T., Sainouchi, M., Kakita, A., Bennett, D. A., Schneider, J. A., ... Colonna, M. (2020). Human and mouse single-nucleus transcriptomics reveal TREM2-dependent and TREM2-independent cellular responses in Alzheimer's disease. *Nature Medicine*, 26, 131–142.

Zuchero, J. B., Fu, M. M., Sloan, S. A., Ibrahim, A., Olson, A., Zaremba, A., Dugas, J. C., Wienbar, S., Caprariello, A. V., Kantor, C., Leonoudakus, D., Lariosa-Willingham, K., Kronenberg, G., Gertz, K., Soderling, S. H., Miller, R. H., & Barres, B. A. (2015). CNS myelin wrapping is driven by actin disassembly. *Developmental Cell*, 34, 152–167.

SUPPORTING INFORMATION

Additional supporting information can be found online in the Supporting Information section at the end of this article.